Chemical Science

ROYAL SOCIETY OF CHEMISTRY

EDGE ARTICLE

View Article Online
View Journal | View Issue

Cite this: *Chem. Sci.*, 2020, **11**, 11740

All publication charges for this article have been paid for by the Royal Society of Chemistry

Near-infrared absorbing Ru(II) complexes act as immunoprotective photodynamic therapy (PDT) agents against aggressive melanoma†

Liubov M. Lifshits, ‡[a] John A. Roque III, ‡[ab] Prathyusha Konda, ‡[c] Susan Monro,[d] Houston D. Cole,[a] David von Dohlen,[b] Susy Kim,[e] Gagan Deep,[e] Randolph P. Thummel,[f] Colin G. Cameron, *[a] Shashi Gujar *[cghi] and Sherri A. McFarland *[a]

Received 15th July 2020
Accepted 4th September 2020

DOI: 10.1039/d0sc03875j

rsc.li/chemical-science

Mounting evidence over the past 20 years suggests that photodynamic therapy (PDT), an anticancer modality known mostly as a local treatment, has the capacity to invoke a systemic antitumor immune response, leading to protection against tumor recurrence. For aggressive cancers such as melanoma, where chemotherapy and radiotherapy are ineffective, immunomodulating PDT as an adjuvant to surgery is of interest. Towards the development of specialized photosensitizers (PSs) for treating pigmented melanomas, nine new near-infrared (NIR) absorbing PSs based on a Ru(II) tris-heteroleptic scaffold [Ru(NNN)(NN)(L)]Cl_n, were explored. Compounds **2**, **6**, and **9** exhibited high potency toward melanoma cells, with visible EC_{50} values as low as 0.292–0.602 μM and PIs as high as 156–360. Single-micromolar phototoxicity was obtained with NIR-light (733 nm) with PIs up to 71. The common feature of these lead NIR PSs was an accessible low-energy triplet intraligand (^{3}IL) excited state for high singlet oxygen ($^1O_2$) quantum yields (69–93%), which was only possible when the photosensitizing ^{3}IL states were lower in energy than the lowest triplet metal-to-ligand charge transfer (^{3}MLCT) excited states that typically govern Ru(II) polypyridyl photophysics. PDT treatment with **2** elicited a pro-inflammatory response alongside immunogenic cell death in mouse B16F10 melanoma cells and proved safe for *in vivo* administration (maximum tolerated dose = 50 mg kg^{-1}). Female and male mice vaccinated with B16F10 cells that were PDT-treated with **2** and challenged with live B16F10 cells exhibited 80 and 55% protection from tumor growth, respectively, leading to significantly improved survival and excellent hazard ratios of ≤0.2.

1. Introduction

Photodynamic therapy (PDT) is an approved anticancer modality where light is used to activate an otherwise nontoxic photosensitizer (PS) to generate cytotoxic reactive oxygen species (ROS) through energy (Type II) or electron (Type I) transfer. Type II formation of $^1O_2$ is thought to be the major contributor to the antitumor photodynamic effect, arising from three synergistic mechanisms: direct cytotoxicity toward tumor cells, damage to tumor vasculature, and induction of an inflammatory response that can stimulate systemic antitumor immunity.[1–13] PDT is delivered in two stages: local or systemic administration of a PS, followed by light delivery to the site of the primary tumor. The light can be delivered virtually anywhere in the body with today's flexible fiber optic devices, and interstitial PDT (i-PDT) techniques can even be used to physically implant the fibers directly inside tumors.[14] The overall PDT response is determined by the PDT regimen, which includes the PS dose as well as the light treatment (wavelength, fluence, and irradiance),[15,16] and can be tuned to enhance local or systemic effects.[16]

[a]*Department of Chemistry and Biochemistry, The University of Texas at Arlington, Arlington, Texas, 76019-0065, USA. E-mail: colin.cameron@uta.edu; sherri.mcfarland@uta.edu*

[b]*Department of Chemistry and Biochemistry, The University of North Carolina at Greensboro, Greensboro, North Carolina 27402, USA*

[c]*Department of Microbiology and Immunology, Dalhousie University, Halifax, Nova Scotia B3H 1X5, Canada. E-mail: shashi.gujar@dal.ca*

[d]*Department of Chemistry, Acadia University, Wolfville, Nova Scotia B4P 2R6, Canada*

[e]*Department of Cancer Biology, Wake Forest School of Medicine, Winston Salem, NC, 27157, USA*

[f]*Department of Chemistry, University of Houston, 112 Fleming Building, Houston, Texas, 77204-5003, USA*

[g]*Department of Pathology, Dalhousie University, Halifax, Nova Scotia B3H 1X5, Canada*

[h]*Department of Biology, Dalhousie University, Halifax, Nova Scotia B3H 1X5, Canada*

[i]*Beatrice Hunter Cancer Research Institute, Halifax, Nova Scotia B3H 4R2, Canada*

† Electronic supplementary information (ESI) available: Methodology, synthetic characterization (1D and 2D NMR, HPLC, HRMS), and (photo)biological data. See DOI: 10.1039/d0sc03875j

‡ Coauthors contributed equally to this work.

The most recent preclinical and clinical studies have shown that, apart from its direct tumor-destroying capacity, PDT can perform immunomodulatory functions. Specifically, PDT stimulates both innate and adaptive immune responses, destroying distant untreated tumor cells (at either primary or metastatic sites) and leading to the development of antitumor immunity that can prevent cancer recurrence.[15,17–28] Such therapy-induced antitumor immunological benefits form the foundation of modern-day cancer immunotherapies. Thus, local PDT has much unrealized promise, and has the potential to be an important adjuvant in multimodal cancer therapy.

Porfimir sodium (Photofrin), a mixture of oligomeric tetrapyrrolic macrocycles that is activated with 630 nm light, was the first approved PS for cancer therapy and remains the gold standard in many PDT applications.[7,29–32] Most second- and third-generation PSs are also based on tetrapyrrole macrocycles (porphyrins, chlorins, bacteriochlorins, and phthalocyanines),[11,33–37] but are single compounds aimed at increasing water solubility, reducing prolonged photosensitivity, and/or improving other properties. Related systems have also been prepared that involve coordination of a central metal ion (*e.g.*, Sn^{IV}, Lu^{III}, Al^{III}, Pd^{II}) to the tetrapyrrole framework to enhance their photophysical and biological properties.[38–42] Only a handful of these next-generation PSs have been approved for clinical use or have advanced to clinical trials.[13]

In a marked departure from these tetrapyrrole macrocycles and their metallated counterparts, we and others have focused on coordination complexes of Ru(II) as light-responsive prodrugs.[38,43–55] Ru(II) has long been at the forefront for many light-based applications due to the rich photophysical and photochemical characteristics of many of its complexes.[11,13,56–68] A wealth of photophysical studies on a variety of Ru(II) polypyridyl complexes over more than several decades has made it possible to tune the excited state dynamics of these systems using rational design principles.[13,69–75] In many systems, the photophysical properties are set by the lowest-energy metal-to-ligand charge transfer (MLCT) excited state. However, judicious choice of ligand combinations around Ru(II) can also lead to accessible excited states that involve predominantly the metal (metal-centered, MC) or one of its ligands (intraligand, IL), each of which has its own characteristic excited state reactivity that can be tailored according to the desired response.

The success of this approach has been demonstrated by our own TLD1433, which is the first Ru(II) PS to advance to human clinical trials.[13] TLD1433 completed a Phase 1b study for treating non-muscle invasive bladder cancer (NMIBC) with PDT in 2018 and proceeded to a Phase 2 study that is currently underway (ClinicalTrials.gov identifiers NCT03053635, NCT03945162). TLD1433 is a Ru(II) polypyridyl complex that incorporates a polarizable π-expansive ligand having a triplet intraligand charge transfer (^{3}ILCT) state energy that is lower than that of the ^{3}MLCT state. This results in a prolonged excited state lifetime due to the significant organic $^3\pi\pi^*$ character of the ^{3}ILCT state that slows competitive intersystem crossing (ISC) back to the ground state. Prolonged triplet state lifetimes are generally longer than 10 μs[74] in the absence of excited state quenchers such as oxygen and tend to promote extremely high $^1O_2$ quantum yields.[76–82]

While many Ru(II) complexes sensitize $^1O_2$ most efficiently with activation in the 400–500 nm wavelength range, we have observed that Ru(II) complexes with π-expansive ligands and lowest-energy ^{3}IL or ^{3}ILCT states can produce $^1O_2$ (and photocytotoxic effects) with 630 nm light despite molar extinction coefficients that are vanishingly small in the red spectral region.[13,80,83] In order to increase the efficiency of this process by increasing molar extinction coefficients and extending the absorption window into the near-infrared (NIR), we have combined π-expanded tridentate ligands with Ru(II) to produce lower-energy MLCT states. These NNN ligands are referred to as chromophoric ligands herein and their π-expansion orthogonal to the direction of the M–N bond is the key feature for extending the absorption window into the NIR. The PDT-active ligand that installs the low-energy ^{3}IL state for efficient $^1O_2$ sensitization is also π-expansive, but extending conjugation along the M–N bond has little effect on the MLCT energy. The challenge in creating NIR-absorbing PSs with high $^1O_2$ quantum yields lies in lowering the energy of the ^{1}MLCT state without lowering the energy of the ^{3}MLCT state below that of the ^{3}IL state. For this we chose the benzo[*i*]dipyrido[3,2-*a*:2′,3′-*c*]phenazine (dppn) ligand due to its exceptionally low-energy ^{3}IL state, estimated at 1.33 eV.[77,84]

Our primary reason for extending the absorption window for Ru(II) complexes that use PDT-active ^{3}IL (or ^{3}ILCT) states was to develop Ru(II)-based NIR PSs for melanoma PDT. Melanoma cells contain melanin, a pigment that is well-adapted for detoxifying ROS[85,86] and that can absorb and attenuate visible light,[87] including the red wavelengths often used for PDT. Although PDT has produced some encouraging results both *in vitro* and *in vivo*[86,88] and in a few isolated clinical cases for melanoma,[85,86,89] pigmented melanomas have proven more resistant to PDT[90] than their amelanotic counterparts.[85,86,91] To improve PDT effectiveness against some of the most aggressive melanomas, we set out to design Ru(II) NIR PSs with high $^1O_2$ quantum yields that could also generate an antitumor immunological response. The longer-term vision is that these NIR PSs may provide immunotherapeutic benefit in optimized PDT regimens delivered alongside surgery.

This study systematically explores combinations of ligands types and Ru(II) with the goal being to achieve NIR PDT effects with a chemically well-defined PS that is stable in the absence of light and has a high $^1O_2$ quantum yield. The core metal-containing scaffold (Chart 1) was inspired by a family of Ru(II) complexes designed as catalysts for water oxidation,[92] where the tridentate 2,2′-(4-(*tert*-butyl)pyridine-2,6-diyl)bis(1,8-naphthyridine) (tpbn) ligand was coordinated to Ru(II) to form robust catalysts with NIR absorption out to approximately 800 nm. We envisioned that this scaffold could be combined with π-expansive PDT-active ligands such as dppn to build PSs for PDT applications that might benefit from the use of NIR light. Herein, we report the results from our structure–activity (SAR) study and identify a novel Ru(II)-based PS platform for achieving PDT with longer wavelengths of light. We also demonstrate that this PDT effect has the potential to create antitumor immunotherapeutic effects *in vitro* and *in vivo*.

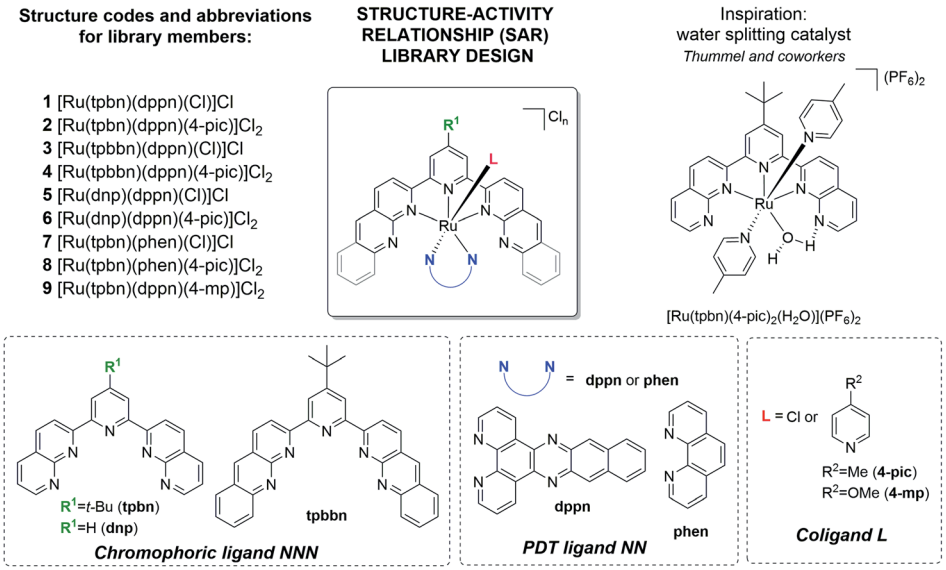

Chart 1 Library design for Ru(II) complexes investigated in this study.

2. Experimental details

Full descriptions of materials, instrumentation, methods, and synthetic details are included in the ESI.†

Ligands 2,2′-(4-(*tert*-butyl)pyridine-2,6-diyl)bis(1,8-naphthyridine) (tpbn),[92,93] 2,2′-(4-(*tert*-butyl)pyridine-2,6-diyl) bis(benzo[*b*][1,8]naphthyridine) (tpbbn),[93,94] and benzo[*i*]dipyrido[3,2-*a*:2′,3′-*c*]phenazine (dppn)[95] were synthesized according literature procedures. Ligand 2,6-di(1,8-naphthyridin-2-yl) pyridine (dnp) was synthesized *via* a Friedlander condensation[96] as described for tpbn[92,93] except that 2,6-diacetylpyridine was used instead of 4-*tert*-butyl-2,6-diacetylpyridine (yield: 99%). The Ru(II) complexes **1–9** have not been reported previously and were characterized by TLC, 1D ^{1}H NMR, 2D ^{1}H–^{1}H COSY NMR (see ESI† for hydrogen assignments), high resolution ESI$^+$ mass spectrometry, and HPLC. The Ru(II) complexes **1–9** were isolated as their Cl$^-$ salts for characterization and biological studies.

[Ru(tpbn)(dppn)(Cl)]Cl (complex **1**) was obtained as a dark-purple powder (conventional heating method: 39%; microwave-assisted method: 30% yield). R_f = 0.61 (alumina; 8% H_2O in acetonitrile). ^{1}H NMR (MeOD-d_3, 500 MHz): δ 10.73 (**d**; dd, J_1 = 5.5 Hz, J_2 = 1.5 Hz, 1H), 10.02 (**f**; dd, J_1 = 8.0 Hz, J_2 = 1.5 Hz, 1H), 9.16 (**g**; s, 1H), 9.16 (**c**; dd, J_1 = 8.0 Hz, J_2 = 1.5 Hz, 1H), 9.11 (**3**; s, 2H), 9.00 (**l**; s, 1H), 8.94 (**3′**; d, J = 8.5 Hz, 2H), 8.54 (**4′**; d, J = 8.5 Hz, 2H), 8.43 (**e**; dd, J_1 = 8.0 Hz, J_2 = 5.5 Hz, 1H), 8.30 (**h**, **k**; m, 2H), 8.27 (**5′**; dd, J_1 = 8.0 Hz, J_2 = 2.0 Hz, 2H), 7.99 (**7′**; dd, J_1 = 4.5 Hz, J_2 = 2.0 Hz, 2H), 7.89 (**a**; dd, J_1 = 5.5 Hz, J_2 = 1.5 Hz, 1H), 7.71 (**i**, **j**; m, 2H), 7.32 (**6′**; dd, J_1 = 8.0 Hz, J_2 = 4.5 Hz, 2H), 7.30 (**b**; dd, J_1 = 8.0 Hz, J_2 = 5.5 Hz, 1H), 1.80 (**4-tBu**; s, 9H). HRMS (ESI$^+$) m/z: [M − Cl]$^+$ calcd for $C_{47}H_{33}ClN_9Ru$ 860.1585; found 860.1573. HPLC retention time: 26.98 min.

[Ru(tpbn)(dppn)(4-pic)]Cl$_2$ (complex **2**) was obtained as a maroon powder (conventional heating method: 81%; microwave-assisted method: 77% yield). R_f = 0.56 (alumina; 8% H_2O in acetonitrile). ^{1}H NMR (MeOD-d_3, 500 MHz): δ 10.08 (**f**; dd, J_1 = 8.5 Hz, J_2 = 1.5 Hz, 1H), 9.47 (**d**; dd, J_1 = 5.5 Hz, J_2 = 1.5 Hz, 1H), 9.32 (**c**; dd, J_1 = 8.0 Hz, J_2 = 1.0 Hz, 1H), 9.20 (**g**; s, 1H), 9.17 (**3**; s, 2H), 9.05 (**3′**; d, J = 8.5 Hz, 2H), 9.02 (**l**; s, 1H), 8.73 (**4′**; d, J = 8.5 Hz, 2H), 8.43 (**e**; dd, J_1 = 8.5 Hz, J_2 = 5.5 Hz, 1H), 8.37 (**5′**; dd, J_1 = 8.0 Hz, J_2 = 2.0 Hz, 2H), 8.36 (**h**/**k**; d, J = 8.0 Hz, 1H), 8.29 (**h**/**k**; d, J = 8.0 Hz, 1H), 8.13 (**7′**; dd, J_1 = 4.0 Hz, J_2 = 2.0 Hz, 2H), 7.80 (**a**; dd, J_1 = 5.5 Hz, J_2 = 1.0 Hz, 1H), 7.72 (**i**, **j**; m, 2H), 7.65 (**2″**; d, J = 7.0 Hz, 2H), 7.45 (**b**; dd, J_1 = 8.0 Hz, J_2 = 5.5 Hz, 1H), 7.43 (**6′**; dd, J_1 = 8.0 Hz, J_2 = 4.5 Hz, 2H), 7.00 (**3″**; d, J = 6.0 Hz, 2H), 2.25 (**4″-Me**; s, 3H), 1.77 (**4-tBu**; s, 9H). HRMS (ESI$^+$) m/z: [M − 2Cl]$^{2+}$ calcd for $C_{53}H_{40}N_{10}Ru$ 459.1235; found 459.1229. HPLC retention time: 23.44 min.

[Ru(tpbbn)(dppn)(Cl)]Cl (complex **3**) was obtained as a dark-green powder (conventional heating method: 30% yield). R_f = 0.57 (alumina; 8% H_2O in acetonitrile). ^{1}H NMR (DMSO-d_6, 700 MHz): δ 10.82 (**d**; dd, J_1 = 4.9 Hz, J_2 = 0.7 Hz, 1H), 10.32 (**f**; dd, J_1 = 8.4 Hz, J_2 = 0.7 Hz, 1H), 9.38 (**g**; s, 1H), 9.34 (**3**; s, 2H), 9.22 (**2′**; d, J = 9.1 Hz, 2H), 9.17 (**9′**; s, 2H), 9.05 (**l**; s, 1H), 8.99 (**c**; dd, J_1 = 7.7 Hz, J_2 = 0.7 Hz, 1H), 8.88 (**1′**; d, J = 9.1 Hz, 2H), 8.79 (**e**; dd, J_1 = 8.4 Hz, J_2 = 4.9 Hz, 1H), 8.44 (**h**/**k**; d, J = 9.1 Hz, 1H), 8.35 (**h**/**k**; d, J = 7.7 Hz, 1H), 8.06 (**5′**; d, J = 8.4 Hz, 2H), 7.96 (**a**; dd, J_1 = 6.3 Hz, J_2 = 1.4 Hz, 1H), 7.77 (**i**/**j**; dd, J_1 = 8.4 Hz, J_2 = 7.0 Hz, 1H), 7.73 (**i**/**j**; dd, J_1 = 7.7 Hz, J_2 = 7.0 Hz, 1H), 7.69 (**7′**; dd, J_1 = 8.4 Hz, J_2 = 7.0 Hz, 2H), 7.50 (**6′**; dd, J_1 = 8.4 Hz, J_2 = 7.0 Hz, 2H), 7.39 (**b**; dd, J_1 = 7.7 Hz, J_2 = 6.3 Hz, 1H), 6.75 (**8′**; d, J = 8.4 Hz, 2H), 1.80 (**4-tBu**; s, 9H). HRMS (ESI$^+$) m/z: [M − Cl]$^+$ calcd for $C_{55}H_{37}ClN_9Ru$ 960.1898; found 960.1896. HPLC retention time: 30.23 min.

[Ru(tpbbn)(dppn)(4-pic)]Cl$_2$ (complex **4**) was obtained as a dark-purple powder (conventional heating method: 66% yield). R_f = 0.49 (alumina; 8% H_2O in acetonitrile). ^{1}H NMR (MeOD-d_3, 700 MHz): δ 10.46 (**f**; d, J = 8.4 Hz, 1H), 9.74 (**d**; d, J = 4.9 Hz, 1H), 9.28 (**3**; s, 2H), 9.21 (**c**; d, J = 7.7 Hz, 1H), 9.18 (**g**; s, 1H), 9.13 (**9′**; s, 2H), 9.05 (**2′**; d, J = 8.4 Hz, 2H), 8.93 (**1′**; d, J =

9.1 Hz, 2H), 8.91 (**l**; s, 1H), 8.83 (**e**; dd, $J_1 = 8.4$ Hz, $J_2 = 5.6$ Hz, 1H), 8.30 (**h/k**; d, $J = 8.4$ Hz, 1H), 8.22 (**h/k**; d, $J = 7.7$ Hz, 1H), 8.02 (**5′**; d, $J = 7.7$ Hz, 2H), 7.88 (**a**; d, $J = 5.6$ Hz, 1H), 7.79 (**2″**; d, $J = 7.0$ Hz, 2H), 7.74 (**7′**; dd, $J_1 = 8.4$ Hz, $J_2 = 7.0$ Hz, 2H), 7.67 (**i, j**; m, 2H), 7.53 (**6′**; dd, $J_1 = 7.7$ Hz, $J_2 = 7.0$ Hz, 2H), 7.43 (**b**; dd, $J_1 = 7.7$ Hz, $J_2 = 5.6$ Hz, 1H), 7.01 (**8′**; d, $J = 8.4$ Hz, 2H), 6.97 (**3″**; d, $J = 6.3$ Hz, 2H), 2.22 (**4″-Me**; s, 3H), 1.81 (**4-tBu**; s, 9H). HRMS (ESI^+) m/z: $[M - 2Cl]^{2+}$ calcd for $C_{61}H_{44}N_{10}Ru$ 509.1391; found 509.1389. HPLC retention time: 25.23 min.

[Ru(dnp)(dppn)(Cl)]Cl (complex **5**) was obtained as a dark-purple powder (conventional heating method: 30%; microwave-assisted method: 26% yield). $R_f = 0.57$ (alumina; 8% H_2O in acetonitrile). ^1H NMR (MeOD-d_3, 700 MHz): δ 10.74 (**d**; dd, $J_1 = 4.9$ Hz, $J_2 = 1.4$ Hz, 1H), 10.03 (**f**; dd, $J_1 = 8.4$ Hz, $J_2 = 1.4$ Hz, 1H), 9.15 (**c**; dd, $J_1 = 7.7$ Hz, $J_2 = 0.7$ Hz, 1H), 9.14 (**g**; s, 1H), 9.09 (**3**; d, $J = 8.4$ Hz, 2H), 8.99 (**l**; s, 1H), 8.81 (**3′**; d, $J = 9.1$ Hz, 2H), 8.54 (**4′**; d, $J = 8.4$ Hz, 2H), 8.45 (**e**; dd, $J_1 = 8.4$ Hz, $J_2 = 4.9$ Hz, 1H), 8.38 (**4**; t, $J = 8.4$ Hz, 1H), 8.29 (**h,k**; m, 2H), 8.27 (**5′**; dd, $J_1 = 7.7$ Hz, $J_2 = 1.4$ Hz, 2H), 8.01 (**7′**; dd, $J_1 = 4.9$ Hz, $J_2 = 1.4$ Hz, 2H), 7.87 (**a**; dd, $J_1 = 5.6$ Hz, $J_2 = 0.7$ Hz, 1H), 7.69 (**i, j**; m, 2H), 7.33 (**6′**; dd, $J_1 = 7.7$ Hz, $J_2 = 4.9$ Hz, 2H), 7.27 (**b**; dd, $J_1 = 7.7$ Hz, $J_2 = 5.6$ Hz, 1H). HRMS (ESI^+) m/z: $[M - Cl]^+$ calcd for $C_{43}H_{25}ClN_9Ru$ 804.0959; found 804.0955. HPLC retention time: 26.09 min.

[Ru(dnp)(dppn)(4-pic)]Cl_2 (complex **6**) was obtained as a purple powder (conventional heating method: 78%; microwave-assisted method: 51% yield). $R_f = 0.43$ (alumina; 8% H_2O in acetonitrile). ^1H NMR (MeOD-d_3, 500 MHz): δ 10.10 (**f**; dd, $J_1 = 8.0$ Hz, $J_2 = 1.0$ Hz, 1H), 9.50 (**d**; dd, $J_1 = 5.5$ Hz, $J_2 = 1.5$ Hz, 1H), 9.32 (**c**; dd, $J_1 = 8.0$ Hz, $J_2 = 1.0$ Hz, 1H), 9.19 (**g**; s, 1H), 9.18 (**3**; d, $J = 8.5$ Hz, 2H), 9.02 (**l**; s, 1H), 8.91 (**3′**; d, $J = 8.5$ Hz, 2H), 8.73 (**4′**; d, $J = 8.5$ Hz, 2H), 8.51 (**4**; t, $J = 8.5$ Hz, 1H), 8.44 (**e**; dd, $J_1 = 8.5$ Hz, $J_2 = 5.5$ Hz, 1H), 8.38 (**5′**; dd, $J_1 = 8.5$ Hz, $J_2 = 2.0$ Hz, 2H), 8.36 (**h/k**; d, $J = 8.0$ Hz, 1H), 8.29 (**h/k**; d, $J = 8.0$ Hz, 1H), 8.15 (**7′**; dd, $J_1 = 4.5$ Hz, $J_2 = 2.0$ Hz, 2H), 7.81 (**a**; dd, $J_1 = 5.5$ Hz, $J_2 = 1.0$ Hz, 1H), 7.72 (**i, j**; m, 2H), 7.65 (**2″**; d, $J = 6.5$ Hz, 2H), 7.44 (**b**; dd, $J_1 = 8.0$ Hz, $J_2 = 5.5$ Hz, 1H), 7.44 (**6′**; dd, $J_1 = 8.0$ Hz, $J_2 = 4.0$ Hz, 2H), 7.00 (**3″**; d, $J = 6.0$ Hz, 2H), 2.25 (**4″-Me**; s, 3H). HRMS (ESI^+) m/z: $[M - 2Cl]^{2+}$ calcd for $C_{49}H_{32}N_{10}Ru$ 431.0922; found 431.0913. HPLC retention time: 22.91 min.

[Ru(tpbn)(phen)(Cl)]Cl (complex **7**) was obtained as a dark-purple powder (conventional heating method: 48% yield). $R_f = 0.57$ (alumina; 8% H_2O in acetonitrile). ^1H NMR (MeOD-d_3, 500 MHz): δ 10.62 (**d**; dd, $J_1 = 5.5$ Hz, $J_2 = 1.5$ Hz, 1H), 9.08 (**3**; s, 2H), 8.90 (**3′**; d, $J = 8.5$ Hz, 2H), 8.89 (**f**; dd, $J_1 = 8.0$ Hz, $J_2 = 1.5$ Hz, 1H), 8.49 (**4′**; d, $J = 8.5$ Hz, 2H), 8.33 (**g**; d, $J = 9.0$ Hz, 1H), 8.29 (**e**; dd, $J_1 = 8.0$ Hz, $J_2 = 5.5$ Hz, 1H), 8.23 (**5′**; dd, $J_1 = 8.0$ Hz, $J_2 = 2.0$ Hz, 2H), 8.07 (**c**; dd, $J_1 = 8.0$ Hz, $J_2 = 1.0$ Hz, 1H), 7.90 (**h**; d, $J = 9.0$ Hz, 1H), 7.75 (**7′**; dd, $J_1 = 4.5$ Hz, $J_2 = 2.0$ Hz, 2H), 7.73 (**a**; dd, $J_1 = 5.5$ Hz, $J_2 = 1.0$ Hz, 1H), 7.31 (**6′**; dd, $J_1 = 8.0$ Hz, $J_2 = 4.0$ Hz, 2H), 7.15 (**b**; dd, $J_1 = 8.0$ Hz, $J_2 = 5.5$ Hz, 1H), 1.78 (**4-tBu**; s, 9H). HRMS (ESI^+) m/z: $[M - Cl]^+$ calcd for $C_{37}H_{29}ClN_7Ru$ 708.1211; found 708.1201. HPLC retention time: 22.74 min.

[Ru(tpbn)(phen)(4-pic)]Cl_2 (complex **8**) was obtained as a dark-purple powder (conventional heating method: 79%; microwave-assisted method: 69% yield). $R_f = 0.45$ (alumina; 8% H_2O in acetonitrile). ^1H NMR (MeOD-d_3, 500 MHz): δ 9.44 (**d**; dd, $J_1 = 5.5$ Hz, $J_2 = 1.5$ Hz, 1H), 9.14 (**3**; s, 2H), 9.01 (**3′**; d, $J = 8.5$ Hz, 2H), 8.94 (**f**; dd, $J_1 = 8.5$ Hz, $J_2 = 1.5$ Hz, 1H), 8.68 (**4′**; d, $J = 8.5$ Hz, 2H), 8.35 (**5′**; dd, $J_1 = 8.5$ Hz, $J_2 = 2.0$ Hz, 2H), 8.32 (**g**; d, $J = 9.0$ Hz, 1H), 8.29 (**e**; dd, $J_1 = 8.5$ Hz, $J_2 = 5.5$ Hz, 1H), 8.19 (**c**; dd, $J_1 = 8.5$ Hz, $J_2 = 1.5$ Hz, 1H), 7.92 (**h**; d, $J = 9.0$ Hz, 1H), 7.92 (**7′**; dd, $J_1 = 4.5$ Hz, $J_2 = 2.0$ Hz, 2H), 7.67 (**a**; dd, $J_1 = 5.5$ Hz, $J_2 = 1.0$ Hz, 1H), 7.66 (**2″**; d, $J = 6.5$ Hz, 2H), 7.42 (**6′**; dd, $J_1 = 8.0$ Hz, $J_2 = 4.5$ Hz, 2H), 7.29 (**b**; dd, $J_1 = 8.0$ Hz, $J_2 = 5.5$ Hz, 1H), 6.97 (**3″**; d, $J = 6.5$ Hz, 2H), 2.23 (**4″-Me**; s, 3H), 1.76 (**4-tBu**; s, 9H). HRMS (ESI^+) m/z: $[M - 2Cl]^{2+}$ calcd for $C_{43}H_{36}N_8Ru$ 383.1047; found 383.1041. HPLC retention time: 18.39 min.

[Ru(tpbn)(dppn)(4-mp)]Cl_2 (complex **9**) was obtained as a maroon powder (conventional heating method: 29%; microwave-assisted method: 66% yield). $R_f = 0.54$ (alumina; 8% H_2O in acetonitrile). ^1H NMR (MeOD-d_3, 500 MHz): δ 10.08 (**f**; dd, $J_1 = 8.0$ Hz, $J_2 = 1.0$ Hz, 1H), 9.49 (**d**; dd, $J_1 = 5.0$ Hz, $J_2 = 1.0$ Hz, 1H), 9.28 (**c**; dd, $J_1 = 8.5$ Hz, $J_2 = 2.0$ Hz, 1H), 9.18 (**3**; s, 2H), 9.17 (**g**; s, 1H), 9.06 (**3′**; d, $J = 8.5$ Hz, 2H), 9.01 (**l**; s, 1H), 8.73 (**4′**; d, $J = 8.5$ Hz, 2H), 8.44 (**e**; dd, $J_1 = 8.0$ Hz, $J_2 = 5.5$ Hz, 1H), 8.37 (**5′**; dd, $J_1 = 8.0$ Hz, $J_2 = 2.0$ Hz, 2H), 8.32 (**h/k**; d, $J = 7.5$ Hz, 1H), 8.28 (**h/k**; d, $J = 8.0$ Hz, 1H), 8.14 (**7′**; dd, $J_1 = 4.0$ Hz, $J_2 = 1.5$ Hz, 2H), 7.79 (**a**; dd, $J_1 = 6.0$ Hz, $J_2 = 1.5$ Hz, 1H), 7.71 (**i, j**; m, 2H), 7.56 (**2″**; d, $J = 7.5$ Hz, 2H), 7.43 (**6′**; b, m, 3H), 6.73 (**3″**; d, $J = 7.0$ Hz, 2H), 3.75 (**4″-OMe**; s, 3H), 1.78 (**4-tBu**; s, 9H). HRMS (ESI^+) m/z: $[M - 2Cl]^{2+}$ calcd for $C_{53}H_{40}N_{10}ORu$ 467.1209; found 467.1199. HPLC retention time: 23.58 min.

3. Results and discussion

3.1 Synthesis and characterization

The inspiration for the NIR Ru(II) scaffold used in our design was the tpbn-bearing Ru(II) complex $[Ru(tpbn)(4\text{-pic})_2(H_2O)](PF_6)_2$ (Chart 1) that was reported by Thummel and coworkers in 2005.[92] Although designed as a water oxidation catalyst for applications in artificial photosynthesis, $[Ru(tpbn)(4\text{-pic})_2(H_2O)](PF_6)_2$ exhibited several key properties that were attractive for PDT. The catalyst was redox active, relatively robust, and absorbed light panchromatically from the UV into the NIR, extending to 800 nm. In addition, substituents on the axial pyridine ligands had a profound influence on the low-energy ^{1}MLCT transitions. The switch from electron withdrawing to electron donating groups at the *para* positions red-shifted the longest wavelength absorption maxima by almost 100 nm. In the present study, we adapted this structure to incorporate a bidentate ligand in the place of the aqua and one of the pyridyl ligands in order to install a π-expansive ligand with a low-energy ^{3}IL state for effective $^1O_2$ sensitization.

The target complexes (**1–9**, Chart 2) of the type $[Ru(NNN)(NN)(L)]Cl_n$ were selected for examining SARs with regard to NIR absorption, $^1O_2$ quantum yields, and *in vitro* PDT effects. Given that the Ru(II) family was designed to have low-energy MLCT states for NIR absorption and that $^1O_2$ generation is most efficient when the ^{3}IL state is below the ^{3}MLCT, the dppn ligand was used as the PDT ligand due to its low-energy ^{3}IL state lying near 1.33 eV.[81,83,97] We hypothesized that there would be a minimum ^{3}MLCT–^{3}IL energy gap required for effective ^{3}IL population that would limit how far into the NIR

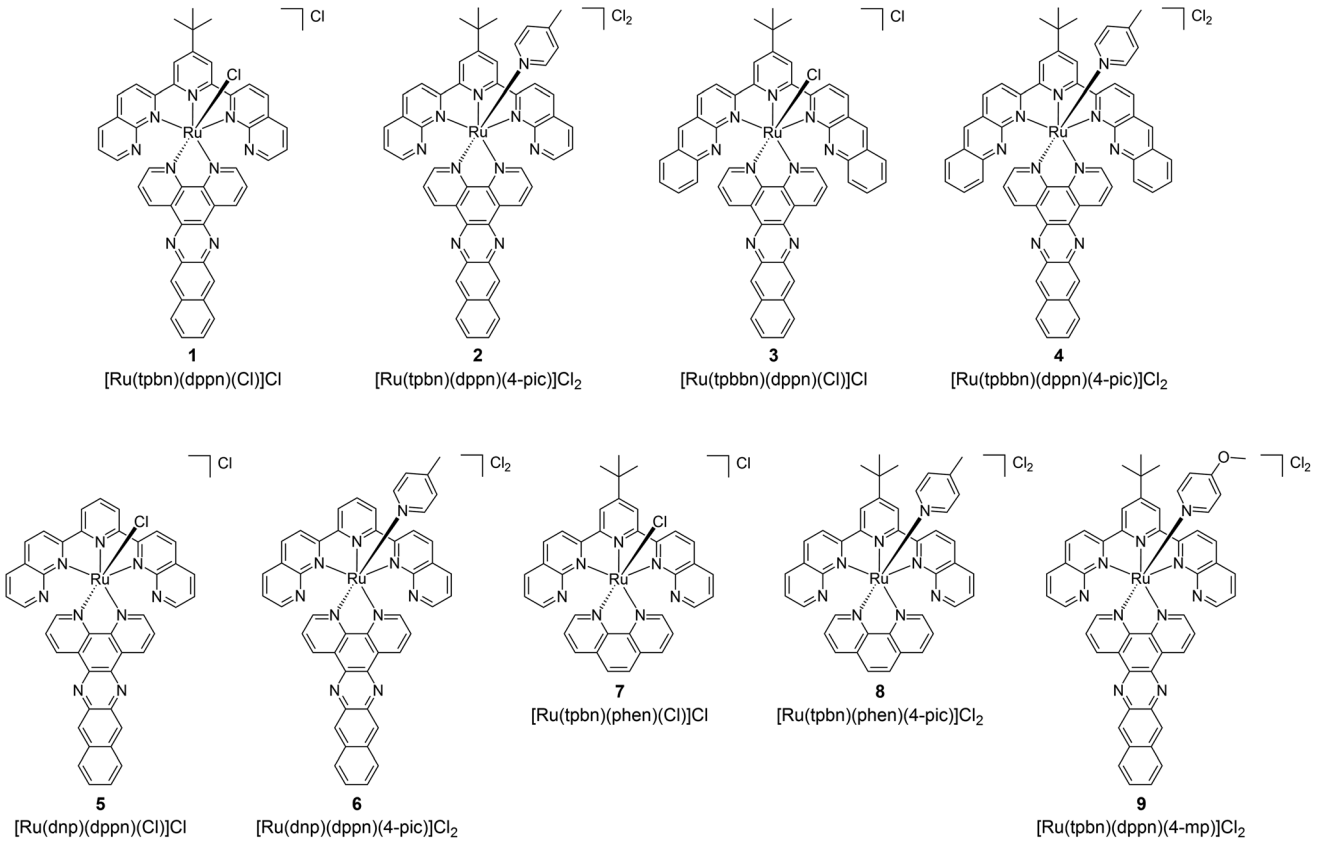

Chart 2 Molecular structures of Ru(II) complexes **1–9**.

the absorption could be shifted while still maintaining high $^1O_2$ quantum yields and good photocytotoxicity.

To demonstrate that the energy of the ^{3}IL state must be below that of the ^{3}MLCT state for activity, the reference compounds **7** and **8**, with 1,10-phenanthroline (phen) in place of dppn, were included since the ^{3}IL state of phen is much higher than the ^{3}MLCT state but the coordination geometry between phen and dppn remains similar. To probe the ^{3}MLCT–^{3}IL energy gap limit by changing the MLCT energy, the chromophoric NNN and the axial (monodentate L) ligands were varied in complexes containing dppn. The NNN ligand tpbbn was used to lower the MLCT states due to its more expanded π-system with distal benzo groups fused to each napthyridine of tpbn. Cl as the axial ligand was also used to lower the MLCT energy. The expectation was that the NIR absorption would red-shift in the following order as a consequence of lowering the MLCT energies: Cl combined with tpbbn (**3**) > Cl combined with tpbn (**1**), 4-pic combined with tpbbn (**4**) > 4-pic combined with tpbn (**2**).

Simple variation to the central pyridine ring of the chromophoric ligand and the axial pyridyl ligands of compound **2** were also explored to determine whether these positions could be used to fine-tune existing properties. Compound **6** contained 2,6-di(1,8-naphthyridin-2-yl)pyridine (dnp) as the chromophoric ligand, which lacked the *t*-Bu group of the tpbn ligand in **2**, and **9** contained 4-methoxypyridine (4-mp) in place of 4-pic in **2**. The corresponding chloro complexes (**5** and **1**, respectively), were also examined given that **1**, **3**, **5** and **7** were synthesized as precursors to the pyridyl complexes. Whereas the pyridyl complexes have an overall charge of +2, the Ru(II) complexes with chloro in the axial position have an overall charge of +1. Complexes **1**, **3**, **5** and **7** and were thus expected to be less water soluble and potentially labile.

Complexes of the formula [Ru(NNN)(NN)(Cl)]Cl **1**, **3**, **5**, **7** were synthesized following a 2-step procedure, similar to what was reported by Thummel and coworkers.[92] $RuCl_3 \cdot 3H_2O$ was refluxed with the NNN chromophoric ligand (tpbn, tpbbn, or dnp) to give the corresponding $[Ru(NNN)](Cl)_3$ species *in situ*, which was then combined (without isolation or purification) with the bidentate NN ligand (dppn or phen) in the presence of TEA to give the [Ru(NNN)(NN)(Cl)]Cl complexes **1**, **3**, **5**, **7** which were purified on neutral alumina to afford the desired products in 30–48% yield. Complexes **1** and **5** were also prepared using microwave irradiation to shorten total reaction time and gave similar yields. Although not tested, it is anticipated that **3** and **7** could also be prepared in much shorter reaction times with microwave irradiation.

The $[Ru(NNN)(NN)(4\text{-pic})]Cl_2$ complexes **2**, **4**, **6**, **8** were synthesized from the corresponding [Ru(NNN)(NN)(Cl)]Cl complexes **1**, **3**, **5**, **7** following a two-step procedure. First, [Ru(NNN)(NN)(Cl)]Cl was refluxed with $AgNO_3$ to facilitate removal of the axial chloride ligand following a modified literature procedure.[98] An excess of 4-pic was then added and the reaction mixture was refluxed to give $[Ru(NNN)(NN)(4\text{-pic})]Cl_2$.

Complexes **2**, **4**, **6**, **8** were purified on neutral alumina, affording final products in 66–81% yield. Complexes **2**, **6** and **8** were also prepared using microwave irradiation to shorten reaction times significantly. In this case, $AgNO_3$ was not required. It is anticipated that **4** could also be prepared in this manner. Complex **9** was synthesized from complex **1** in a similar approach as for **2**, except 4-mp was used in place of 4-pic and was likewise successfully prepared using microwave irradiation.

Complexes **1–9** were characterized by high resolution ESI^+ mass spectrometry (Fig. S29–S37†), 1D ^1H NMR and 2D ^1H–^1H COSY NMR spectra (Fig. S1–S28†), and HPLC (Fig. S38–S46†). The molecular ion peaks matching the calculated $[M - Cl]^+$ peaks were observed for [Ru(NNN)(NN)(Cl)]Cl complexes **1**, **3**, **5**, **7**. Likewise, molecular ion peaks matching the calculated $[M - 2Cl]^{2+}$ peaks were observed for $[Ru(NNN)(NN)(4\text{-pic})]Cl_2$ complexes **2**, **4**, **6**, **8** and for $[Ru(tpbn)(dppn)(4\text{-mp})]Cl_2$ complex **9**, confirming the correct molecular masses of the complexes. Observed molecular ions exhibited isotopic patterns characteristic of mononuclear Ru(II)-containing complexes, with separation of 1 *m*/*z* between the peaks for M^+ ions and 0.5 *m*/*z* between the peaks for M^{2+} ions.

To confirm structures, the 1D ^1H NMR and 2D ^1H–^1H COSY NMR spectra of complexes **1–9** (Fig. S1–S28†) were closely analyzed and all hydrogens assigned. Assignments were made based on connectivity observed by 2D ^1H–^1H COSY NMR, coupling constants observed in 1D ^1H NMR spectra, and precedent assignments of similar systems reported in the literature.[93,99] The process of assigning the signals in each ^1H NMR spectrum for complexes **1–9** is described in detail in the ESI.†

3.2 Photophysical characterization

3.2.1 Absorption properties. The compounds within the series were panchromatic absorbers from the UV into the NIR, with the NIR cut-off determined by the ligand combinations in a predictable manner. Generally, the electronic transitions in these complexes could be grouped into three or four wavelength regions (Fig. 1). Below 400 nm, ligand-localized $^1\pi\pi^*$ transitions involving the polypyridyl groups of the NNN, NN, and N ligands gave rise to intense, sharp bands with large molar extinction coefficients (10^4 to 10^5 M^{-1} cm^{-1}).[69,73,100,101] Spectra for compounds containing the dppn ligand included additional ligand-localized $^1\pi\pi^*$ bands ($\varepsilon \approx 10^4$ M^{-1} cm^{-1}) with characteristic fine structure between 370–430 nm contributed by transitions typical of azaaromatics.[81] Much broader and less intense bands ($\varepsilon \approx 10^3$ to 10^4 M^{-1} cm^{-1}) due to ^{1}MLCT transitions involving Ru(dπ) orbitals and ligand π* orbitals of the polypyridyl groups appeared between 400–650 nm.[69,73,102–104] The longer wavelength ^{1}MLCT bands ($\varepsilon \leq 10^3$ M^{-1} cm^{-1}) that occurred beyond 650 and into the NIR were assigned to Ru(dπ) → π* transitions involving increased π-delocalization onto the distal polypyridyl groups of the NNN chromophoric ligands.[94,105–107]

The longest wavelength absorption maxima in the NIR was dictated by the ligand combinations around Ru(II) and ranged from 715 to 903 nm. Generally, chloro as the monodentate ligand and tpbbn as the NNN chromophoric ligand produced the largest bathochromic shifts of the NIR ^{1}MLCT transitions, while pyridyl as the monodentate ligand and tpbn as the NNN chromophoric ligand resulted in the smallest shifts. The largest red-shifts result from an increase in the energies of the Ru(dπ) orbitals (due to the weak-field chloro monodentate ligand) and a concomitant decrease in the energies of the ligand-based π* orbitals (with more extended π-conjugation in the tpbbn chromophoric ligand) as exemplified by **3** having the longest NIR absorption maximum in the series at 903 nm and **2** having the shortest at 715 nm.

Combining the chloro ligand with the smaller chromophoric tpbn ligand (**1**, **7**) or 4-pic with the larger chromophoric tpbbn ligand (**4**) resulted in NIR maxima (805–820 and 785 nm, respectively) that were intermediate between these two extremes. Minor changes to the substituents on the central pyridyl ring of the smaller chromophoric ligand, *e.g.*, dnp, (**1** *vs.* **5**, **2** *vs.* **6**) or on the monodentate pyridyl ligand (**2** *vs.* **9**) produced only minor shifts in these bands. Likewise, the bidendate NN ligand in this series (dppn or phen) had little influence on these maxima (**1** *vs.* **7**, **2** *vs.* **8**) despite dppn being much more π-extended compared to phen, supporting the notion that the π* orbitals involved in the NIR MLCT transitions of complexes containing dppn involve only the proximal portion of this ligand.

Together, the absorption studies highlight that the $[Ru(NNN)(NN)(L)]Cl_n$ scaffold selected for this investigation represents a reliable system for tunable NIR absorption, where local maxima can be shifted over 200 nm in the NIR, from 700 to 900 nm. Course tuning (50–100 nm) was achieved by controlling (i) whether L was a weaker- or stronger-field ligand, and (ii) the degree of π-expansion for the NNN chromophoric ligand. Fine-tuning (<20 nm) was demonstrated through substituent modifications to the tpbn and 4-pic ligands of **2** (Fig. 2). The pyridyl complexes combined with the smaller chromophoric NNN ligand (**2**, **6**, **8**, and **9**) exhibited better solubility and did not undergo ligand dissociation during the course of the absorption

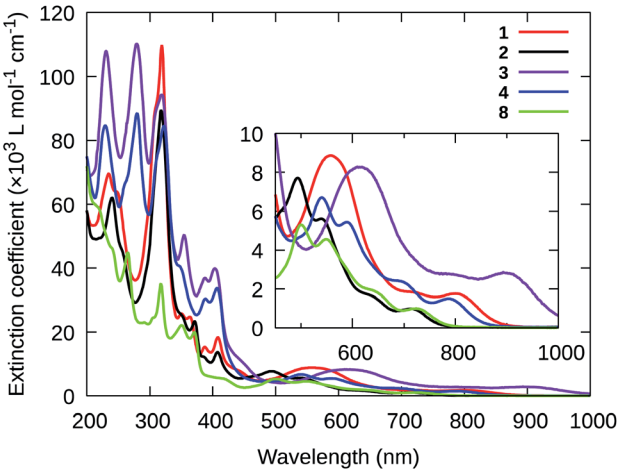

Fig. 1 Steady-state UV-vis absorption spectra of compounds **1–4** and **8** (20 μM in MeCN).

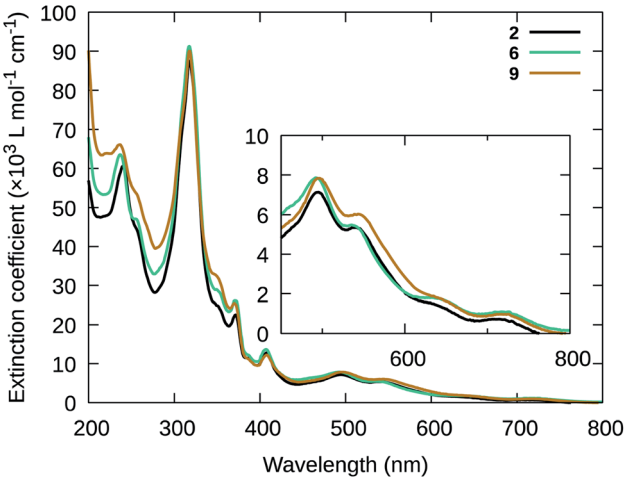

Fig. 2 Steady-state UV-vis absorption spectra of compounds **2**, **6**, and **9** (20 μM in MeCN).

measurements (as was observed for the chloro complexes). Therefore, these complexes were preferred for additional spectroscopic and biological studies. Their higher-energy NIR MLCT transitions could also be advantageous for maximizing $^1O_2$ sensitization. Nevertheless, the chloro and tpbbn complexes (**1**, **3**, **4**, **5**, and **7**) were included in some of the subsequent studies to better understand the activities of the favored compounds.

3.2.2 Transient absorption spectroscopy. The excited states of the pyridyl complexes (**2**, **4**, **6**, **8–9**) were interrogated by transient absorption (TA) spectroscopy using a 355 nm excitation pulse (Fig. 3). The TA profiles are differential spectra derived from positive signals (arising from excited state absorption) that are superimposed on negative signals (arising from the ground state bleach). They offer an opportunity to extract information on lowest-energy excited state configurations and lifetimes. Compounds combining the tpbn chromophoric (NNN) ligand with dppn produced the characteristic spectral signature of the dppn-based ^{3}IL excited state with a maximum near 550 nm,[77] while compounds **4** and **8** did not. The excited state decays for **4** and **8** were dominated by signals with lifetimes on the order of tens of nanoseconds (attributed to ^{3}MLCT relaxation), while **2**, **6**, and **9** decayed biexponentially with a short component that was similar to that observed for **4** and **8** (assigned as ^{3}MLCT relaxation) but also a longer component that reflected contributions from the dppn-based ^{3}IL state.

While the longer lifetimes were on the order of hundreds of nanoseconds and shorter than the microsecond ^{3}IL lifetimes in Ru(II) diimine complexes such as $[Ru(bpy)_2(dppn)]^{2+}$, the intense and broad transient with a maximum near 550 nm in the TA spectra displayed the characteristic signature of the dppn-based ^{3}IL excited state.[77] These shorter lifetimes for the ^{3}IL state in **2**, **6**, and **9** were attributed to substantial mixing with the low-energy ^{3}MLCT states in these systems. The absence of this signature in **8**, which lacked the dppn ligand and thus a low-energy ^{3}IL state, provided further support of this assignment. The lack of the ^{3}IL signature in the TA spectrum of **4**,

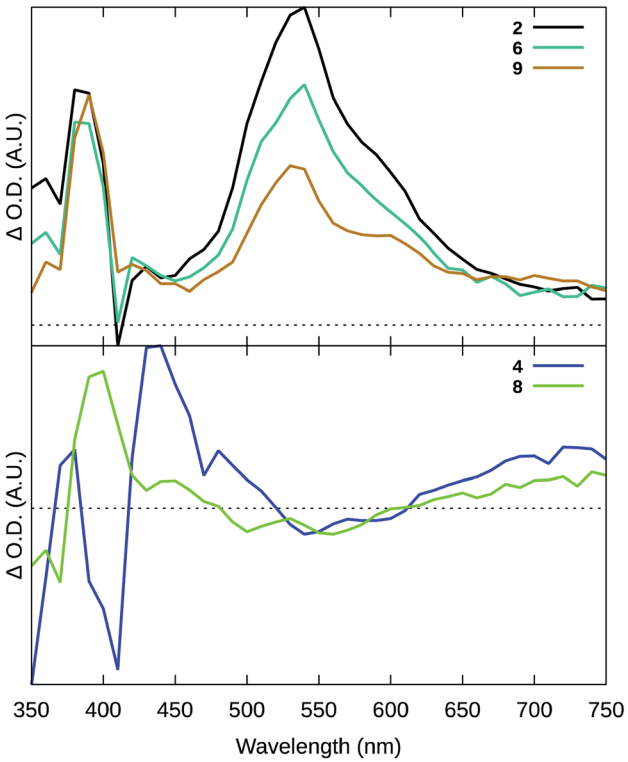

Fig. 3 Transient absorption (TA) spectra collected for selected compounds using λ_{ex} = 355 nm (t = 0, 20 ns integration), 20 μM in degassed MeCN.

which does incorporate the dppn ligand, was attributed to a much lower-energy ^{3}MLCT state afforded by the more π-extended tpbbn chromophoric ligand. This lower energy was reflected in an ^{3}MLCT lifetime for **4** that was twice as short as the corresponding ^{3}MLCT decay for the other pyridyl-based complexes. Together, the TA data suggests that the Ru(II) complexes containing the tpbn chromophoric ligand and dppn lead to effective population of ^{3}IL states within this family. It was anticipated that these longer-lived ^{3}IL states would be better poised to sensitize $^1O_2$.

3.2.3 Singlet oxygen quantum yields. The $^1O_2$ quantum yields (Φ_Δ) for the complexes were calculated relative to $[Ru(bpy)_3](PF_6)_2$ by direct measurement of $^1O_2$ phosphorescence in acetonitrile with excitation at 630 nm and 753 nm (Table 1). These excitation wavelengths were chosen based on those used clinically for Photofrin (630 nm) and TOOKAD Soluble (753 nm). Values for Φ_Δ were also determined using the maxima from excitation scans collected at λ_{em} = 1270 nm (if different from the two clinical wavelengths). Despite the chloro ligand being somewhat labile in MeCN, the $^1O_2$ quantum yields are included for these complexes (only initial scans with fresh solutions were used in order to limit error due to sample degradation during the measurement). All of the chloro complexes (**1**, **3**, **5**, and **7**) were poor $^1O_2$ generators, with Φ_Δ values less than 10%, with the exception of **5**, where the value for Φ_Δ was 28% using the excitation maximum at 464 nm but <10% at the clinical wavelengths.

Table 1 Spectroscopic data and singlet oxygen quantum yields (Φ_Δ) for complexes **1–9**

Cmpd	λ_{abs}/nm (log(ε/M^{-1} cm^{-1}))	τ_{TA}/ns ($\lambda_{\tau_1} \rightarrow \tau_n$/nm)	Φ_Δ (λ_{ex}/nm)
1	234 (4.76), 318 (4.94), 365 (4.31), 409 (4.18), 560 (3.87), 805[a] (3.18)	n.d.	0.04[b] (630), 0.02 (753)
2	240 (4.79), 318 (4.95), 371 (4.37), 406 (4.12), 493 (3.88), 540 (3.75), 636 (3.22), 715[a] (2.98)	59 ns, 564 ns (380) 59 ns, 563 ns (540)	0.93[b] (630), 0.86 (753)
3	230 (4.91), 278 (4.92), 319 (4.85), 354 (4.58), 402 (4.48), 610 (3.80), 903[a] (3.31)	n.d.	0.05[b] (464), 0.01 (630), 0.03 (753)
4	229 (4.93), 279 (4.95), 322 (4.93), 350 (4.60), 386 (4.48), 406 (4.53), 540 (3.83), 785[a] (3.18)	36 ns (380) 30 ns (410) 33 ns (440) 29 ns (540)	0.14[b] (455), 0.09 (630), 0.03 (753)
5	233 (4.47), 250 (4.43), 318 (4.66), 366 (4.04), 405 (3.91), 436 (3.63), 813[a] (2.85)	n.d.	0.28[b] (464), 0.09 (630), 0.07 (753)
6	237 (4.80), 255 (4.66), 318 (4.95), 371 (4.41), 408 (4.13), 493 (3.89), 725[a] (3.02)	120 ns, 334–367 ns (380) 81 ns, 340–411 ns (540)	0.77 (630), 0.82[b] (640), 0.34 (753)
7	224 (4.65), 266 (4.53), 319 (4.37), 364 (4.18), 406 (3.71), 553 (3.67), 821[a] (3.12)	n.d.	0.06[b] (455), 0.04 (630), 0.05 (753)
8	264 (4.74), 318 (4.63), 350 (4.44), 370 (4.39), 416 (3.83), 501 (3.82), 725[a] (3.08)	62 ns (400) 62 ns (560)	0.17[b] (455), 0.10 (630), 0.10 (753)
9	237 (4.91), 318 (5.09), 370 (4.48), 406 (4.25), 498 (4.00), 725[a] (3.12)	67–79 ns, 358–384 ns (390) 357–361 ns (530)	0.69 (630), 0.75[b] (632), 0.69 (753)

[a] Longest wavelength absorption maximum. [b] Maximum singlet oxygen quantum yield.

Complexes containing the tpbn, or related dnp, chromophoric ligand combined with dppn and a pyridyl-based monodentate ligand (**2**, **6**, **9**) gave the largest $^1O_2$ quantum yields. Compound **2**, derived from 4-pic, was the most efficient producer of $^1O_2$ ($\Phi_\Delta = 93\%$ with $\lambda_{ex\ max} = 630$ nm and 86% with $\lambda_{ex} = 753$ nm). The $[Ru(NNN)(dppn)(N)]^{2+}$ scaffold tolerated changes to either the 4-position of the central pyridine (**6**) or monodentate pyridine-based ligand (**9**) with only a slight loss of efficiency for $^1O_2$ production, with the exception **6** exhibiting a wavelength dependence and suffering a loss in efficiency at 753 nm ($\Phi_\Delta = 0.34$) compared to 630 nm ($\Phi_\Delta = 0.77$).

By contrast, the pyridyl-based complexes derived from the π-expanded tpbbn ligand (**4**) or lacking the dppn ligand (**8**) were poor $^1O_2$ generators, with values of Φ_Δ near 10% or less using the longer (clinical) wavelengths and only slightly higher when excited at their excitation maxima (14 and 17%, respectively). These were also the two pyridyl complexes that lacked the dppn-based ^{3}IL transient in their TA spectra and exhibited only the shorter ^{3}MLCT lifetime.

Complexes **2**, **6**, and **9** were the complexes that had the largest $^1O_2$ quantum yields, displayed the characteristic ^{3}IL signature, and had the longest excited state lifetimes. These observations suggest that the presence of the longer-lived excited state lifetime exhibited by **2**, **6**, and **9** is correlated with larger quantum yields for $^1O_2$ sensitization. Thus, we assign efficient $^1O_2$ production to the accessible ^{3}IL state identified in TA spectra for the Ru(II) complexes containing tpbn, dppn, and a pyridyl-based monodentate ligand. We anticipated that such complexes based on this scaffold, with accessible and longer-lived ^{3}IL states, would be most active for PDT.

3.3 Photobiological studies

3.3.1 Cellular assays. The dark and light cytotoxicities for **1–9** were measured in three melanoma lines growing as 2D adherent monolayers. The cell lines were chosen to represent different sexes (male human SKMEL28 *vs.* female human A375) and species (murine B16F10 *vs.* human SKMEL28 and A375) since our *in vivo* work would use a murine line. They also differ in their pigmentation (melanotic B16F10), aggressiveness, and melanosome stages.[108,109] Briefly, cells growing in log phase were seeded, dosed with compound (1 nM to 300 μM), and then incubated for 48 h before cell viability was determined using the resazurin assay for cytotoxicity. To determine photocytotoxicity, an analogous set of plates were prepared but were irradiated 16–19 h after compound addition. Dose–response curves were prepared from both dark and light conditions and analyzed to provide dark and light EC_{50} values, the effective concentration to reduce relative viability by 50%. Phototherapeutic indices (PIs), or the light-induced amplification of cytotoxicity, were calculated as the ratios of the dark EC_{50} values to the light EC_{50} values. Specialized treatment protocols (hypoxia, light dosimetry, immunology, *etc.*) are described as they are discussed.

Across the family, compounds with +1 charge (*i.e.*, those containing the anionic chloro monodentate ligand) aggregated in aqueous solutions of high ionic strength. The chloro compounds were labile at room temperature in some

coordinating solvents, did not display the desirable ^{3}IL signature in the TA spectra, and had low $^1O_2$ quantum yields. By contrast, compounds with +2 charge (*i.e.*, those containing the neutral pyridine-based monodentate ligand) were readily water-soluble and stable in coordinating solvents under ambient conditions. Family members with substituted pyridines (4-pic, 4-mp) combined with dppn as the bidentate ligand exhibited the desired ^{3}IL TA signature and had the highest $^1O_2$ quantum yields. Therefore, we focused on the substituted pyridine-based compounds (**2**, **6**, **9**) as the most suitable members for photobiological studies, but compared to their chloro counterparts and other reference compounds when appropriate.

3.3.2 Dark cytotoxicity. The dark cytotoxicities for the nine compounds in all three cell lines are illustrated in the activity plots shown in Fig. 4 (black filled circles) and tabulated in Tables S4–S6.† The dark EC_{50} values ranged from 15 to 256 μM in the SKMEL28 cell line, with compound **1** being the most cytotoxic and **7** being the least (both chloro compounds). The range for the pyridine-based counterparts was smaller, from approximately 50 to 130 μM where **4** was the most cytotoxic and **8** the least. The dark cytotoxicity in both chloro and pyridine compounds roughly paralleled lipophilicity for soluble compounds (Fig. S48†).

Using compound **2** as a reference point because it had the highest $^1O_2$ quantum yield ($\Phi_\Delta = 0.93$) and potential as a phototherapeutic lead, we were interested in comparing dark cytotoxicity in terms of SARs for **2** and its close relatives. Replacing 4-pic in **2** with the anionic chloro ligand as in **1** reduced the charge on the Ru(II) compound from +2 to +1 and increased the dark toxicity by seven-fold. Expanding the chromophoric ligand in **2** by fusing two additional benzene rings as in **4** doubled the dark cytotoxicity. Removal of the *t*-Bu group of the central pyridine ring of the chromophoric ligand in **2** as in **6**, replacing dppn with phen as in **8**, or changing 4-pic to 4-mp as in **9** had only a modest effect. Replacing dppn for phen in **8** decreased dark toxicity whereas the other two modifications in **6** and **9** slightly increased toxicity. A closer look at lipophilicities within this comparison group (Fig. S48 and Table S1†) reveals a significant correlation between dark cytotoxicity in SKMEL28 and lipophilicity. Correlation in either A375 or B16F10, however, was not significant. The general trends are the same for A375 and B16F10 but with subtle distinctions. Changing the pyridine ligand as in **9** relative to **2** brings their dark toxicities within error of each other in the additional lines. Instead of doubling the toxicity, the expanded chromophore in compound **4** only slightly increased toxicity from **2** (51.1 *vs.* 62.6 μM) in A375. Additionally, compounds with dppn are more cytotoxic in A375 than either SKMEL28 or B16F10 while those with phen (**7**, **8**) are much less cytotoxic.

Generally, compounds with the lowest dark cytotoxicity (largest EC_{50} values) are most desirable as phototherapeutic compounds. Excluding the chloro compounds, which had other

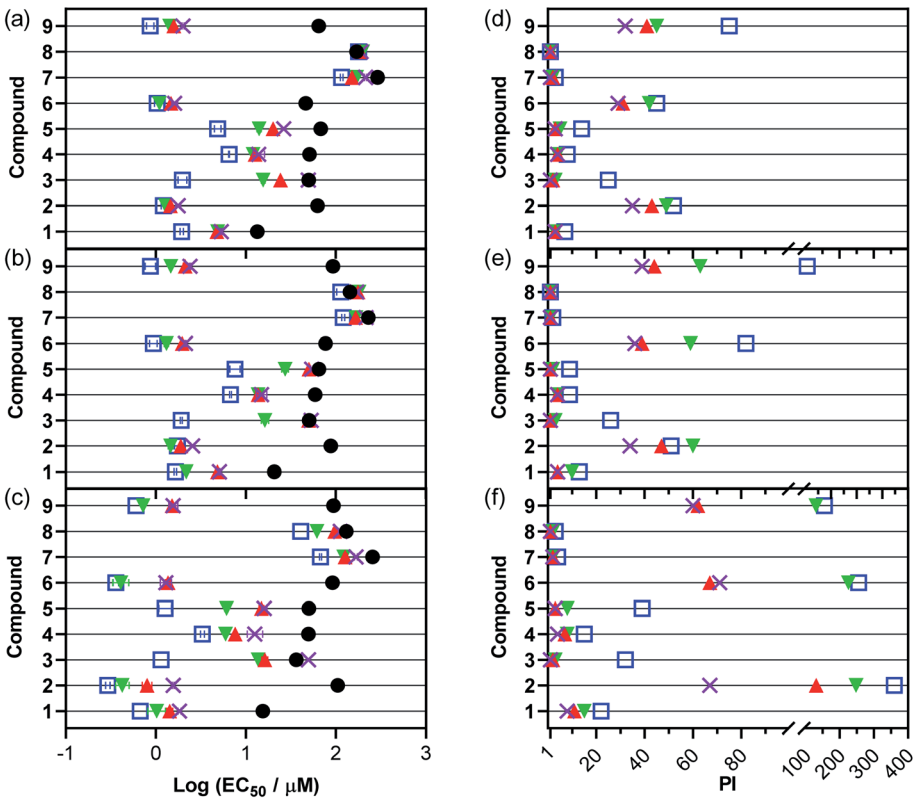

Fig. 4 *In vitro* cytotoxicity and photocytotoxicity dose–response parameters in A375 (a and d), B16F10 (b and e), and SKMEL28 (c and f) melanoma cell lines with compounds **1–9**. Treatments include dark (0 J cm^{-2}; black circles) and 100 J cm^{-2} doses of 733 nm (purple cross), 633 nm (red triangle), 523 nm (green inverted triangle), and visible (peak maxima ~450 nm; open blue square). Plots (a–c) show Log (EC_{50} ± SEM) and (d–f) show PI, where PI is the ratio of dark to light EC_{50} values. All linear-scale values are listed in the ESI.†

undesirable properties, the pyridine-based compounds **2**, **6**, **8**, and **9** were the least dark toxic toward all three melanoma cell lines (dark EC_{50} values $\geq$ 46.3 μM) with their magnitude and order of toxicity not deviating significantly between the lines. Of these, **2**, **6**, and **9** had the largest $^1O_2$ quantum yields (and displayed the characteristic ^{3}IL TA signature for dppn) and thus might be expected to exhibit the widest phototherapeutic margins.

3.3.3 Photocytotoxicity. The photocytotoxicities of the compounds in the series were assessed using 100 J cm^{-2} doses of broadband visible (400–700 nm, 19 mW cm^{-2}), green (523 nm, 18.5 mW cm^{-2}), red (633 nm, 20 mW cm^{-2}) and NIR (733 nm, 9 mW cm^{-2}) light. The spectral output of the applied light sources are shown in Fig. S49.† Comparisons of the photocytotoxicity values are shown in Fig. 4.

With light activation, the cytotoxicities exerted by the compounds increased by as much as 360-fold. The extent of light amplification depended on the wavelength(s) used and the particular compound, with shorter wavelengths (*e.g.*, visible irradiation containing significant contributions from the bluer wavelengths) generally producing greater light-related cytotoxicity. Light of any wavelength had very little effect on the cytotoxicity of compound **8**, which contained phen as the bidentate ligand instead of dppn, and confirmed that both the high $^1O_2$ quantum yield and long ^{3}IL state lifetime imparted by the dppn ligand were crucial for generating phototoxic effects.

Compounds **2**, **6**, and **9**, having the highest $^1O_2$ quantum yields and the characteristic ^{3}IL state signature in their TA spectra, were the most phototoxic compounds in the series across all light treatments and all cell lines. Light EC_{50} values toward the SKMEL28 cell line ranged from 0.292 μM to 0.602 μM with broadband visible light, from 0.407 μM to 0.720 μM with 523 nm green light, from 0.798 μM to 1.52 μM with 633 nm red light, and from 1.29 μM to 1.56 μM with 733 nm NIR light. The order of potency toward SKMEL28 generally was **2** > **6** > **9**, but with a few discrepancies in the trend depending on wavelength. The A375 and B16F10 melanoma cell lines proved to be slightly more resistant, but compounds **2**, **6**, and **9** were still the most photocytotoxic. In both B16F10 and A375 the order of potency reversed with **9** > **6** > **2** being the general trend. Interestingly, the wavelength-dependence for photocytotoxicity appeared to be different across the three cell lines and also between compounds. For example, compound **2** in A375 and B16F10 exhibited almost no difference in its EC_{50} values between the visible and 733 nm NIR treatments. For comparison, the difference between the visible and NIR EC_{50} values for **2** in SKMEL28 was 5-fold.

3.3.4 Phototherapeutic indices (PIs). The structural variations that led to lower dark cytotoxicities also resulted in the best photocytotoxicity profiles with all wavelengths in all three cell lines. Therefore, the PIs, which are the true measure of light-induced cytotoxicity, were the largest for these three compounds as well. Across all cell lines, the order of PI potency for **2**, **6**, and **9** varied based on wavelength. Their PI values in SKMEL28 ranged from 156 to 360 with visible light, 131 to 248 with 523 nm light, 62 to 132 with 633 nm light, and 60 to 71 with 733 nm light treatments. The general order of compound potency by PI for **2**, **6**, and **9** largely followed their light EC_{50} values. In the more resistant lines, PIs were attenuated by 50% or more. For example, in the most resistant line A375, values ranged from 52 to 75 with visible light and 29 to 35 with 733 nm light, with both 523 and 633 nm falling between these two ranges. The attenuated activity in A375 and B16F10 could be due to a combination of their greater endogenous defenses against ROS, differences in melanosome stages and overall pigmentation, and/or greater aggressiveness compared to SKMEL28.[108,109]

Although the PI values were somewhat attenuated at 733 nm compared to the other light treatments, the fact that **2**, **6**, and **9** had sizeable PIs with NIR light means that we can now push the activation of Ru(II) systems beyond the red/far-red wavelengths (630–670 nm) that had been the limit for single-photon PDT with Ru(II) polypyridyl complexes. Our orthogonal strategy for accessing the NIR window with polypyridyl complexes has been to combine Os(II) with π-expanded ligands and was described by us for $[Os(biq)_2(NN)]Cl_2$ in 2017. We used a high fluence at 808 nm (600 J cm^{-2}) to achieve PI values between 6 and 12 in human U87 glioblastoma and HT1376 bladder cancer cell lines.[110] While these compounds were NIR active, certain characteristics limited their utility and suited them as model systems for later generations. More recently, we have reported an Os(II) complex ($[Os(phen)_2(IP\text{-}4T)]Cl_2$, where IP-4T is imidazo[4,5-*f*][1,10]phenanthroline appended with quaterthiophene) with a submicromolar light EC_{50} value and PI of 77 at 733 nm.[111] Our choice of 733 nm for the present Ru(II) series is still within the PDT window and produces greater activity than that reported for the $[Os(biq)_2(NN)]Cl_2$ examples (71 *vs.* 12) with 800 nm activation (Fig. 6) and is of similar activity to our recently reported $[Os(phen)_2(IP\text{-}4T)]Cl_2$. To our knowledge, the present series gives the largest NIR PIs (60–71) for Ru-based photosensitizers without the use of special measures such as two photon absorption[68] or upconverting nanoparticles.[112]

The PI values of the nine compounds investigated were significantly correlated to their $^1O_2$ quantum yields, demonstrating the potential role of ROS as the mediator for cell death. Fig. 5 shows the correlation of $^1O_2$ quantum yield and PI in the

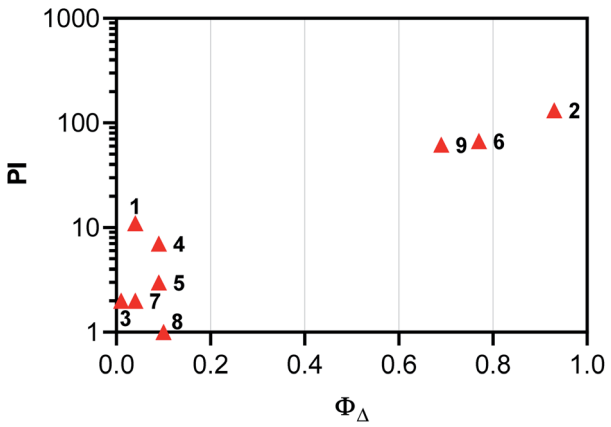

Fig. 5 Correlation plot of PI and Φ_Δ for SKMEL28 cells using 633 nm illumination or excitation, respectively.

SKMEL28 cell line using 630 nm, the clinically approved wavelength used for Photofrin. Two clusters were apparent: (i) compounds with the lowest $^1O_2$ quantum yields that had the smallest PI values, and (ii) compounds with the highest $^1O_2$ quantum yields that also had the largest PI values.

To confirm the critical role of oxygen in the observed photoactivity, we screened the family under low oxygen tension using SKMEL28 cells (where the compounds exhibited the largest PI values under normoxia). $[Ru(bpy)_2(dppn)]Cl_2$ was included as an internal control for oxygen-dependence because it has a comparably high $^1O_2$ quantum yield ($\Phi_\Delta = 0.75$ in MeCN), similar to compounds **2**, **6**, and **9**, but is not photoactive in 1% hypoxia.[77,79,81,113] Regardless of the light treatment, the compounds lost almost all of their photocytotoxicity toward SKMEL28 cells (PIs ≤ 3) at 1% oxygen (Table S7†). Although not tested, a similar loss of activity would be expected in the more resistant cell lines. This absolute dependence on molecular oxygen suggests that these compounds exert their photocytotoxic effects through ROS-based mechanisms.

While the pyridyl complexes such as **2**, **6**, and **9** were completely stable to ligand dissociation at 37 °C for extended periods of time in the absence of a light trigger, 100 J cm^{-2} doses of broadband visible (400–700 nm, 19 mW cm^{-2}), green (523 nm, 18.5 mW cm^{-2}), red (633 nm, 20 mW cm^{-2}) and NIR (733 nm, 9 mW cm^{-2}) light resulted in changes to the UV-vis and HPLC spectra of the complexes that were consistent with dissociation of the monodentate pyridyl ligand to form the aquated product and free ligand as well as oxidation[83] of the dppn ligand. The quantum yields for these competing photochemical pathways were not determined, but the amount of photoproduct formed was related qualitatively to photon energy where visible light resulted in the most photoproduct and NIR the least. The photosubstitution pathway, which might be expected to lead to oxygen independent photocytotoxicity, did not yield any photocytotoxic effects in hypoxia. Likewise, the PIs were highly correlated to $^1O_2$ quantum yields. These observations point toward a very minor role, if any, for the photosubstitution pathway.

3.3.5 Validation. Given the variability that can result in cellular assays across laboratories using different assay methods, cells of different passage number, and culture conditions, we assayed the top three compounds in two different cell lines (B16F10 and SKMEL28) across two additional laboratories (Dalhousie University and Acadia University) by two different researchers (Konda and Monro) using slightly different assay conditions (noted in experimental). The dark cytotoxicities were greater at both Dalhousie and Acadia Universities, likely due to a longer (1 day) total incubation period. Compounds **2** and **6** were similar in their dark EC_{50} values while **9** had 2- to 3-fold greater toxicity in SKMEL28 and B16F10, respectively. While the PIs were smaller when **2**, **6**, and **9** were tested elsewhere, they were still active. Visible PIs were comparable for all three compounds in SKMEL28 cells. Discrepancies arose for 630 nm treatments regarding compound **9** with a two-fold smaller PI at Dalhousie University in B16F10 and two-fold greater PI values for compounds **6** and **9** at Acadia University in SKMEL28. In light of these efforts, compounds **2**, **6**, and **9** remained strong candidates for further photobiological study.

3.3.6 Photocytotoxicity at higher light doses. The light sources used in the standard dose–response assay described previously are limited in the irradiances that can be delivered to an entire microplate. In order to control the irradiance more precisely and to explore higher fluences and irradiances, we performed photocytotoxicity experiments using the Modulight illumination system (ML8500, Modulight Inc.) which has the unique feature of well-by-well illumination using different light conditions. In Fig. 6 compound **2** is highlighted for its panchromatic activity in SKMEL28 from 455 to 810 nm. Higher fluences were required with longer wavelengths (namely, 753 and 810 nm), and 976 nm was ineffective regardless of the fluence (data not shown). The high fluences and irradiances used in these light treatments did not cause any loss in cell viability in the absence of compound (Fig. S50†). All light treatments with **2** reduced cell viability by ≥60% down to 2.5 μM except for 810 nm, where lower activity correlated with photon energy as described earlier (Fig. 4). The most potent effects were obtained with 455 to 630 nm (EC_{50} = 0.5 to 1 μM), followed by 753 nm (EC_{50} = 2.02 μM), and lastly 810 nm with roughly 10 to 20% viability reduction compared to dark controls between 2.5 and 10 μM. Compounds **6** and **9** followed similar trends. Compound **2** maintained its potency at the higher irradiances, where PDT effects can be reduced due to PDT-induced oxygen depletion in more advanced tissue or 3D models.[114–116]

3.3.7 Photocytotoxicity at lower light doses. The effects of lower fluence and irradiance were examined with the light sources used in Fig. 4 (visible, 523 nm, 633 nm, and 733 nm). For all three compounds and light treatments (Fig. S51–54†), photocytotoxicity could be maintained at lower fluence or irradiance. Fluences 1/20 to 1/2 of that used for the data shown in Fig. 4 (5 to 50 J cm^{-2} *vs.* 100 J cm^{-2}) yielded single micromolar activity (Fig. 7). Notably, the Modulight's 20 nm longer 753 nm treatment (Fig. 6) provided comparable cell kill, between

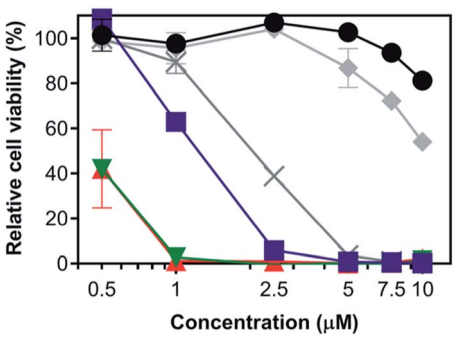

Fig. 6 Panchromatic PDT example of compound **2** in SKMEL28 cells at high irradiance from 455–810 nm using the ML8500 platform. Values shown are in duplicate and are the mean ± standard deviation (SD). Treatments include dark (black circle, 0 J cm^{-2}), 455 nm (blue square, 25 J cm^{-2}, 100 mW cm^{-2}), 525 nm (green inverse triangle, 100 J cm^{-2}, 300 mW cm^{-2}), 630 nm (red triangle, 200 J cm^{-2}, 300 mW cm^{-2}), 753 nm (grey X, 200 J cm^{-2}, 300 mW cm^{-2}), 810 nm (grey diamond, 400 J cm^{-2}, 400 mW cm^{-2}). Light-only controls are available in Fig. S50.†

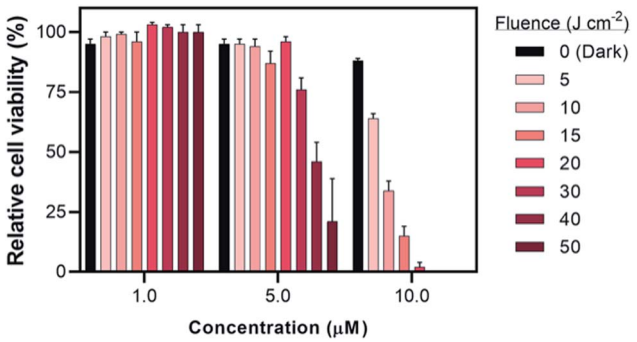

Fig. 7 Fluence dependence (±SD) of compound **2** against SKMEL28 cells with 733 nm treatment at 10 mW cm^{-2} and fluences ranging from 0–50 J cm^{-2}.

1–5 μM, as the 733 nm condition in Fig. 7. For added perspective, treatment times were the same or up to ten times longer in Fig. 7 compared to the high fluence and high irradiance applied in the 753 nm treatment in Fig. 6. The question arose whether the compound activity would improve at low irradiance as reported in some PDT examples.[115,117]

The contrast in activities between the three leads **2**, **6**, and **9** became clearer at 10 J cm^{-2} with varying irradiance between 2–10 mW cm^{-2} (Fig. S53–S54†). At this low fluence, a stronger wavelength dependence was observed with increasing potency in the order of 733 nm < 633 nm < 523 nm ≤ vis. In general, increased irradiance resulted in increased activity for these leads in SKMEL28. We only tested their irradiance dependence across a small range, however, and further study is required to probe how far this dependence extends, whether it increases asymptotically or plateaus below the maximum tested values of 100–400 mW cm^{-2}. This is only a limited example of the compound behavior, since other models (*e.g.*, tissue, *ex vivo*) would require their own dosimetry optimizations.

3.3.8 Maximum tolerated dose (MTD). Compound **2** was chosen for additional longer-term studies. In preparation, its safety profile in mice was determined according to the metric of maximum tolerated dose (MTD) in a dose-escalation study using intraperitoneal injection (IP). Observable toxicity was only

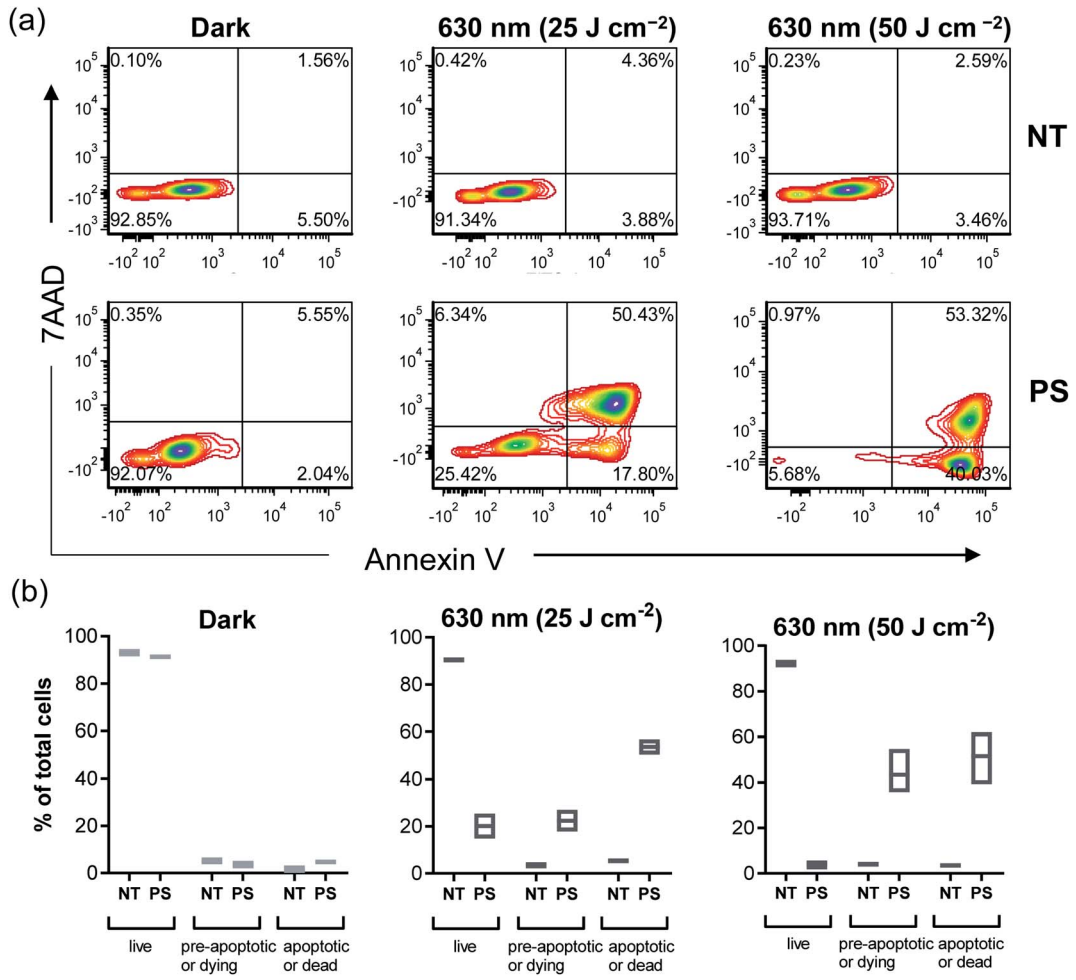

Fig. 8 Compound **2**-PDT induces cell death in B16F10 melanoma cell line. (a and b) *In vitro* cell death analysis using Annexin V – 7AAD flow cytometry assay. Contour plots are depicted in (a) where the lower left quadrant represents live cells, lower right represents pre-apoptotic cells, upper left represents necrotic cells, and upper right represents apoptotic or dead cells. Top panel of (a) is non-treated (NT) and bottom panel is PS-treated (PS). Corresponding data to (a) is represented as box plots in (b).

apparent at the higher doses 75–100 mg kg^{-1}. The MTD was determined to be 50 mg kg^{-1} and acceptable for *in vivo* immunological experiments.

3.4 Immunogenic potential of compound 2-mediated PDT (2-PDT)

It is becoming more evident in the realm of cancer research that there is an urgent need to develop therapies that do not simply kill cancer cells but also induce an immunological response against the tumor to confer long term protection and prevent relapse. Given the importance of the immunological response in melanoma, compound **2** was selected for further investigation of its immunological potential as a PDT agent. The B16F10 mouse melanoma cell line was used for *in vitro* characterization since this is the cell line that would be used for subsequent *in vivo* immunological studies in a syngeneic mouse model. In this cell line, the EC_{50} and PI_{630} values for compound **2** activated by clinically-approved 630 nm light were approximately 1.40 μM and 37, respectively, using a fluence of 100 J cm^{-2} and irradiance of 22.8 mW cm^{-2}. Cell death analysis (with Annexin-V/7AAD staining by flow cytometry), using this EC_{50} value but with a fluence of 25 or 50 J cm^{-2} (22.8 mW cm^{-2}), revealed the existence of pre-apoptotic (Annexin-V +ve/7AAD −ve)[118] and apoptotic (Annexin-V +ve/7AAD +ve)[118] populations alongside some smaller fraction of live B16F10 cells (Fig. 8a and b) where **2** in the absence of light treatment showed no dark cytotoxicity. Therefore, 1.40 μM was determined to be a suitable concentration to use for the subsequent immunological experiments, which require some fraction of live and pre-apoptotic cells for analysis.

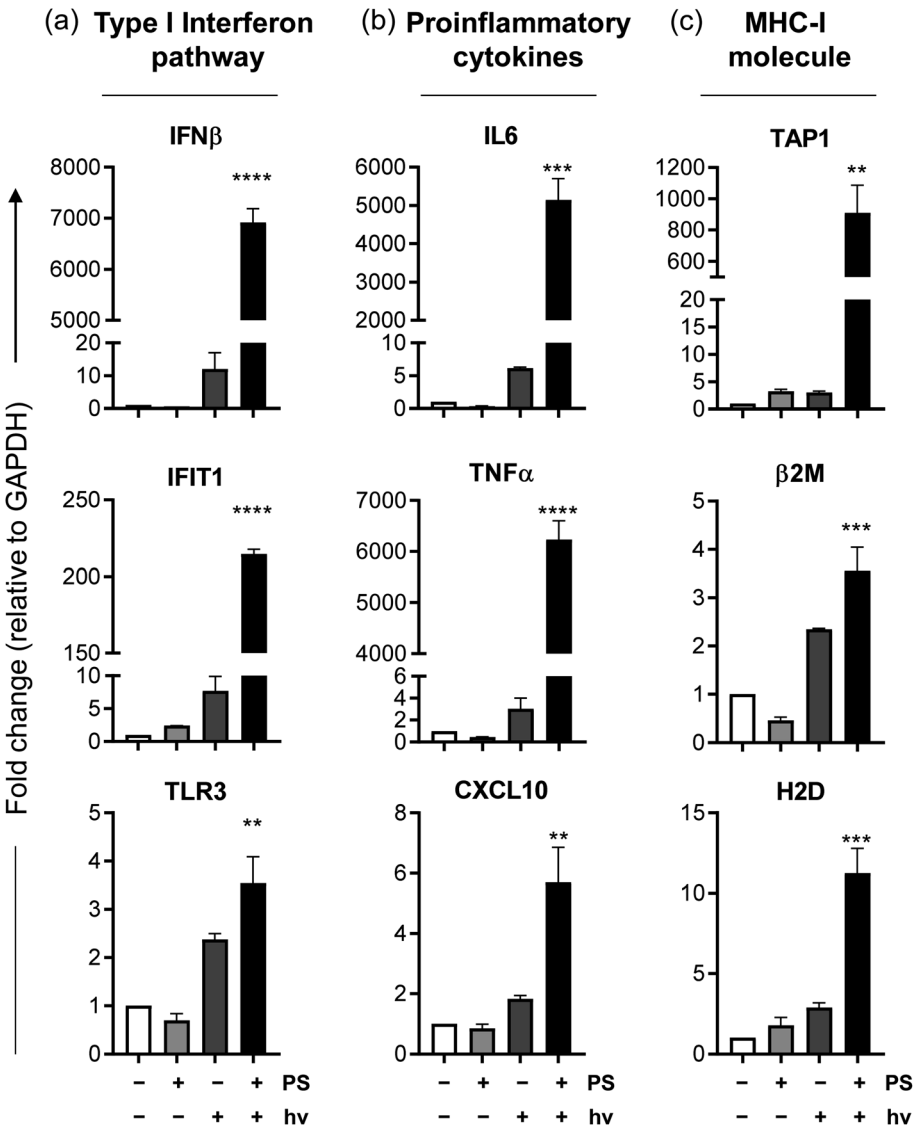

Fig. 9 Compound **2**-PDT stimulates multiple immunological pathways *in vitro*. qRT-PCR analysis of B16F10 cells untreated, treated only with compound-**2**, only light or treated with both compound **2** and light (**2**-PDT), for genes associated with (a) type 1 interferon pathway (IFNβ, IFIT1, TLR3); (b) proinflammatory cytokines (IL6, TNFα, CXCL10); (c) antigen presentation – MHC-I molecule (TAP1, β2M, H2D). Fold changes represented relative to untreated samples and normalized to control gene, GAPDH.

3.4.1 Pro-inflammatory immune response with 2-PDT. Cancers harbor suppressive microenvironment in which the antitumor immune responses are dampened *via* various immune evasion strategies. Thus, therapies which overturn such cancer-associated immunosuppression go on to induce clinically desired antitumor immunity. In this context, the effect of compound **2**-PDT on the expression of various immunological markers known to be involved in inflammatory processes in B16F10 melanoma cells was examined. As revealed by quantitative real-time polymerase chain reaction (qRT-PCR) analysis, compound **2**-PDT upregulated the gene expression of several type I interferon pathway molecules (IFNβ, IFIT1, and TLR3; Fig. 9a),[119–121] proinflammatory cytokines (IL6, TNFα, and CXCL10; Fig. 9b),[119–121] and molecules involved in antigen presentation (TAP1, β2M, and H2D; Fig. 9c)[121,122] in the B16F10 melanoma cell line. While some of these markers were also upregulated with only light treatment in the absence of the compound, the level was significantly lower compared to treatment with compound **2**-PDT. These results indicate that **2**-PDT promotes a strong pro-inflammatory immune response in the B16F10 melanoma cell line, which is a prerequisite to the initiation of innate and adaptive antitumor immunity.

3.4.2 Immunogenic cell death induction (ICD) with 2-PDT. The process of therapy-driven generation of antitumor immunity is often preceded by 'immunogenic' death of cancer cells. Considering the pro-inflammatory effects of **2**-PDT, we then explored whether the photocytotoxicity by **2**-PDT involved any immunological mechanisms with a focus on the process of immunogenic cell death (ICD) through a multifaceted analysis of diverse immunological parameters. First, ROS induction as well as endoplasmic reticulum (ER) stress-induced ER chaperone expression[123–128] was examined following **2**-PDT. Flow cytometry analysis captured the induction of ROS molecules at both the cellular and mitochondrial level (Fig. 10a), and qRT-PCR analysis revealed an increase in the

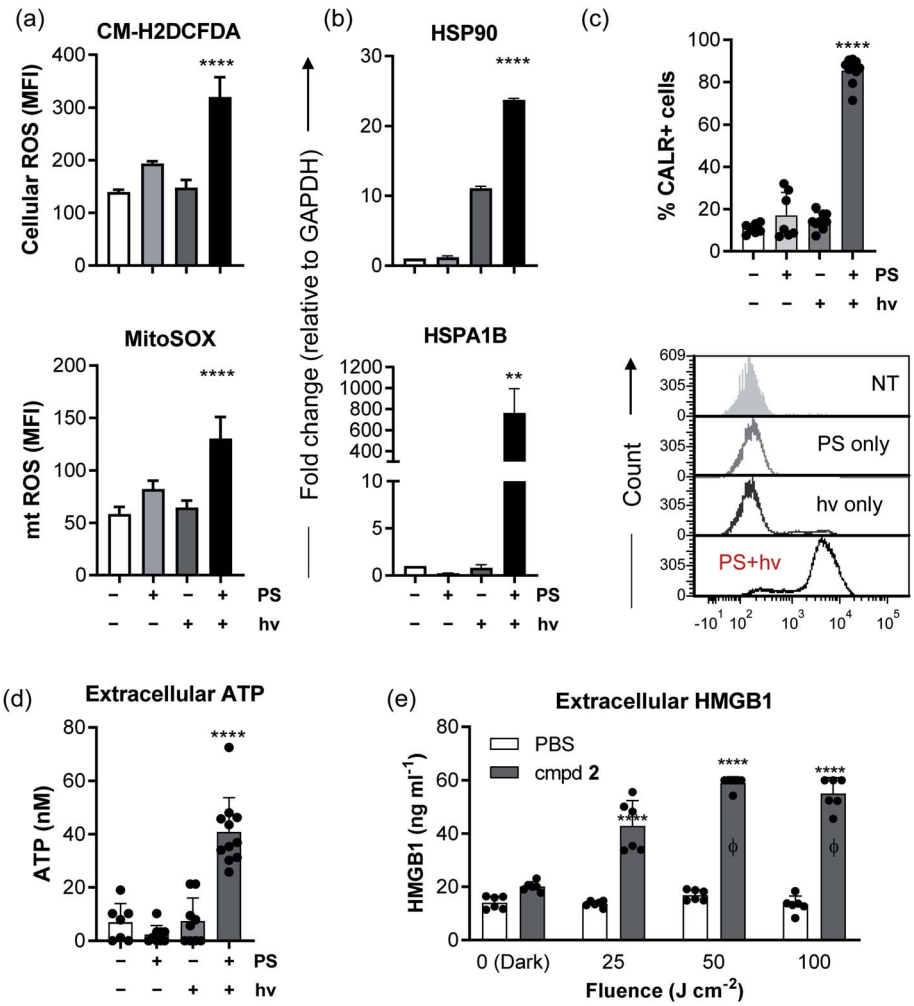

Fig. 10 **2**-PDT induces immunogenic cell death in B16F10 melanoma model *in vitro*. (a) Mean fluorescence intensity of ROS analysis with flow cytometry 4 h post compound **2**-PDT for cellular ROS (CM-H_2DCFDA) and mitochondrial ROS (MitoSOX). (b) qRT-PCR analysis of ER chaperones HSP90 and HSPA1B 12 h post-**2**-PDT in B16F10 cells *in vitro*. (c) Analysis of surface expression of ER chaperone Calreticulin using flow cytometry 4 h post-**2**-PDT in B16F10 cells *in vitro*. Representative histograms associated with the bar graph (c, bottom). (d) Extracellular ATP analysis 12 h post-**2**-PDT in B16F10 cells *in vitro*. (e) Analysis of HMGB1 release from B16F10 cells *in vitro* 24 h post-**2**-PDT. Treatment conditions represent no treatment, PS only, light only, PS and light (**2**-PDT). Φ = sample beyond upper limit of detection in (e), >60 ng mL^{-1}

gene expression of ER chaperones HSP90 and HSPA1B (Fig. 10b). Together, these data showed that **2**-PDT induced ROS and cell stress—key hallmarks of ICD—in cancer cells.

Other important ICD hallmarks were also assessed, including damage-associated molecular patterns (DAMPs) such as the translocation of ER chaperone calreticulin (CALR) to the plasma membrane, secretion of adenosine triphosphate (ATP), and release of high mobility group box 1 protein (HMGB1) extracellularly.[121] The effect of **2**-PDT on CALR, HMGB1 and ATP[121] in B16F10 cells was tested at various time points, with those time points producing optimal expression of ICD markers highlighted in Fig. 10. Flow cytometry analysis of B16F10 cells 4 h post-**2**-PDT showed a significant increase in surface calreticulin expression compared to nontreated (NT) cells or cells treated with PS or light only (Fig. 10c) alongside extracellular release of ATP 12 h post-treatment (Fig. 10d). A significant increase in extracellular HMGB1 was also detected in the supernatant collected from the cells 24 h post **2**-PDT (Fig. 10e). These results suggest that **2**-PDT-treated B16F10 cells trigger DAMPs associated with ICD. Together, these analyses demonstrate that compound **2**-PDT-induced photocytotoxicity in B16F10 melanoma cells is accompanied by ICD.

3.4.3 Effects of vaccination with 2-PDT treated B16F10 cells on melanoma progression *in vivo*. The therapeutic relevance of **2**-PDT induced ICD *in vitro* was examined *in vivo* with an immuno-competent, syngeneic B16F10 tumor model. The gold standard approach to evaluate the therapeutic and anticancer potential of ICD consists of vaccination with the *in vitro*-treated, ICD-undergoing cancer cells followed by a challenge with the live cancer cells of the same antigenic origin.[121] B16F10 cells were treated with **2**-PDT and ICD-undergoing cells collected at 4 h and 12 h post-**2**-PDT were combined for the vaccination. Either PBS- or **2**-PDT-treated B16F10 cells were injected subcutaneously (SC) into the left flank of C57BL/6 female and male mice. The mice were then challenged with untreated B16F10 cells by injection into the right flank. These mice were assessed for tumor growth and survival (Fig. 11a).

Female and male C57BL/6 mice that received the vaccination showed either no tumor growth or reduced tumor growth as compared to unvaccinated mice (Fig. 11b–d). This analysis showed either delayed or no tumor growth with 80% protection

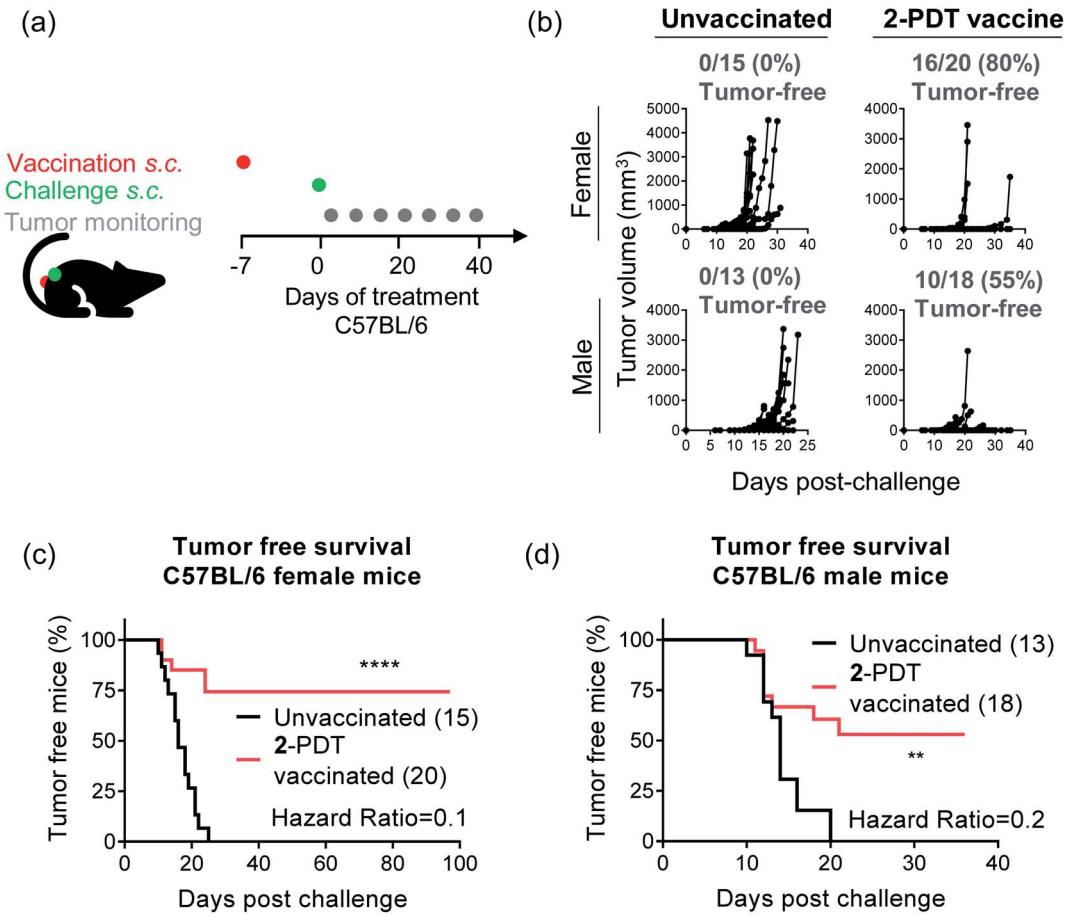

Fig. 11 Compound **2**-PDT induced immunogenic cell death confers protection against rechallenge *in vivo* in B16F10 mouse melanoma model. (a) Schematic representation of the *in vivo* mouse experiment. C57BL/6NCrl mice were injected with PBS or compound **2**-PDT treated B16F10 cells (vaccination) and challenged with untreated B16F10 cells 7 days post-vaccination on the opposite flank and monitored for tumor growth and survival. (b) Tumor growth curves for unvaccinated and vaccinated female and male mice. Each line represents one mouse. (c and d) Tumor free survival curves of unvaccinated and vaccinated C57BL/6NCrl female (c) and male mice (d).

from tumor growth in female mice and 55% protection in male mice. Survival studies revealed a significant improvement of tumor-free survival in vaccinated female and male mice as compared to unvaccinated mice (Fig. 11c and d). Hazard ratios, which estimate treatment risk, were strongly favorable with values of 0.1 for females and 0.2 for males, denoting low risk for mice treated with the **2**-PDT vaccine. Given that the vaccination and challenge injections were done on bilateral flanks, this data indicates an abscopal effect and generation of systemic immunity. Together, these data confirm the induction of ICD with **2**-PDT in the B16F10 syngeneic mouse melanoma model and also highlight differences in the PDT-induced antitumor response based on the sex of the mice.

It is becoming increasingly apparent that biological sex determines the progression and therapeutic outcomes in several cancers.[129] In the context of melanoma, men have a higher incidence as well as mutation burden compared to women[130,131] It has also been noted that men and women show varied responses and outcomes to cancer therapies like checkpoint blockade therapy.[132–139] In congruence, we observed that the percentage of melanoma tumor-free mice following vaccination was greater in female mice and that tumor survival rates were also higher for this cohort.

While tumor growth itself was comparable in unvaccinated female and male mice, differences in tumor development and survival in the vaccinated groups suggest that there may be variations in immune responses elicited by female and male mice toward B16F10 melanoma. Sex-dependent biases in immune responses to both self-antigens and foreign antigens have previously been documented in both animal models as well as in humans, with an overall higher innate and adaptive immune responses in women as compared to men.[129,140,141] In the context of C57BL/6 mice, female mice display superior tumor-specific $CD8^+$ T cell responses against B16F10 melanoma in response to checkpoint inhibitor therapy compared to male mice.[133] Similar sex-biased differences have also been reported in pro-inflammatory and anti-inflammatory cytokines associated with various stages of B16F10 melanoma development in female and male C57BL/6 mice.[142] We believe that similar variations in tumor-specific immune responses are responsible for the sex-biased differences observed in our study. Further characterization is required to outline the underlying differences in sex-biased immune parameters for **2**-PDT.

4. Conclusions

This multi-dimensional study defines the SARs for achieving the requisite photophysical properties to elicit PDT effects with NIR-absorbing Ru(II)-based PSs. All of the investigated compounds exhibited NIR absorption beyond 700 nm, which was tunable over 200 nm. Combining the tpbbn chromophoric ligand with the chloro axial ligand (**3**) led to the longest NIR absorption (λ_{max} = 900 nm) that extended past 1000 nm. The smaller chromophoric tpbn ligand combined with the axial chloro ligand (**1**, **5**, **7**) or the combination of the larger tpbbn ligand and the pyridyl monodentate ligand (**4**) blue-shifted the NIR maximum to 790–800 nm, and the smaller tpbn ligand combined with the pyridyl axial ligand (**2**, **6**, **9**) resulted in λ_{max} near 720 nm. The identity of the bidentate ligand (phen *versus* dppn) had little impact on the NIR absorption profiles of otherwise identical complexes.

The absorption studies underscored that the pyridyl complexes combined with the smaller chromophoric tpbn ligand (**2**, **6**, **9**) had higher stabilities and better aqueous solubilities. Structural modifications to the axial monodentate pyridyl ligand or the central pyridyl group of the tpbn chromophoric ligand were well tolerated and did not substantially impact the energies or relative molar extinction coefficients of the major electronic transitions observed for this sub-family. Therefore, R_1 and R_2 (Chart 1) represent convenient handles for fine-tuning the chemical, biological, and photophysical properties of this new structure class while maintaining NIR absorption.

Compared to the rest of the compounds, **2**, **6**, and **9** had the largest $^1O_2$ quantum yields by a wide margin. A detailed photophysical investigation revealed that these were the only compounds with accessible ^{3}IL states. Given that the NIR absorption is set by the energies of the MLCT states and that $^1O_2$ is generated most effectively from ^{3}IL states, there exists a fundamental limit with regard to how much the MLCT state energies can be lowered without compromising the PDT effect. In other words, the ^{3}MLCT state cannot be lower in energy than the ^{3}IL state, which explains why the $^1O_2$ quantum yields for **2**, **6**, and **9** were largest and also suggests that in the present system, the ^{3}MLCT–^{3}IL energy gap, estimated at 0.22 eV, is sufficient for ^{3}IL population. This assertion was also corroborated in the *in vitro* cellular studies where **2**, **6**, and **9** gave the largest PI values, regardless of the wavelengths of light used in the investigated melanoma cell lines. Importantly, wavelengths longer than 700 nm yielded photocytotoxic effects with single-digit micromolar EC_{50} values.

These compounds lost activity in hypoxia, pointing toward PDT (*e.g.*, ROS) as the source of photocytotoxicity. Given the immunostimulatory potential of PDT and the importance of the immune response for melanoma outcomes, compound **2** was selected for further investigation in this context. Treatment of B16F10 melanoma cells with **2**-PDT stimulated immunological responses and resulted in a significant upregulation of several immune-associated genes from the type 1 interferon pathway, proinflammatory cytokines, and the antigen-presentation pathway. **2**-PDT also induced both mitochondrial and cellular ROS alongside a significant upregulation of ER chaperones HSP90 and HSPA1B gene expression, translocation of calreticulin to the plasma membrane, and secretion of ATP and HMGB1 into the extracellular media. These results confirmed that compound **2**-PDT induces bonafide ICD markers *in vitro*.

The immunogenicity of **2**-PDT was also confirmed in a syngeneic mouse model *in vivo*. Vaccination with **2**-PDT treated B16F10 cells conferred protection against tumor growth upon challenge with live B16F10 cells, statistically improving tumor-free survival in female and male vaccinated mice as compared to the unvaccinated group. These results also indicate the generation of systemic immunity as revealed from the abscopal effect. The percentage of melanoma tumor-free mice following vaccination as well as overall survival rates were

greater for females, underscoring that tumor-specific immune responses may be responsible for the sex-biased differences that have been observed clinically with regard to melanoma incidence, mutation burden, and response to therapy.

This study shows that **2**-PDT (with clinically-approved red light) destroys melanoma cells directly as well as indirectly by ICD-mediated generation of anti-tumor immune responses. Additional studies are underway to explore the optimum PDT regimen (including NIR wavelengths) and to delineate the therapeutic potential and understand the different immune cell mediators involved. Overall, these results identify compound **2** as a PS that could potentially be used for eliciting systemic effects through local delivery of melanoma PDT.

Ethical statement

In vivo experimental procedures were approved by the Dalhousie University Animal Ethics Committee in accordance with the regulations/guidelines from the Canadian Council on Animal Care (CCAC; protocol number 18-151).

Conflicts of interest

S. A. M. has a potential research conflict of interest due to a financial interest with Theralase Technologies, Inc. and PhotoDynamic, Inc. A management plan has been created to preserve objectivity in research in accordance with UTA policy.

Acknowledgements

S. A. M., C. G. C., S. G., R. P. T., and G. D. thank the National Cancer Institute (NCI) of the National Institutes of Health (NIH) (Award R01CA222227) for support. The content in this article is solely the responsibility of the authors and does not necessarily represent the official views of the National Institutes of Health. S. A. M. also thanks Dr Daniel Todd as UNCG's Triad Mass Spectrometry Facility manager and his assistants Jennifer Simpson and Diane Wallace. S. A. M. likewise thanks Dr Franklin Moy for his experimental support and instrument maintenance as UNCG's NMR facility manager. S. A. M. notes that the graphical (TOC) abstract was created with https://www.BioRender.com.

References

1 *Photodynamic Therapy: Basic Principles and Clinical Applications*, ed. B. W. Henderson and T. J. Dougherty, Dekker, New York, 1992.
2 T. J. Dougherty, C. J. Gomer, B. W. Henderson, G. Jori, D. Kessel, M. Korbelik, J. Moan and Q. Peng, Photodynamic Therapy, *J. Natl. Cancer Inst.*, 1998, **90**(12), 889–905, DOI: 10.1093/jnci/90.12.889.
3 R. Bonnett, *Chemical Aspects of Photodynamic Therapy; Advanced chemistry texts*, Gordon and Breach Science Publishers, Amsterdam, The Netherlands, 2000.
4 *Advances in Photodynamic Therapy: Basic, Translational, and Clinical*, ed. M. R. Hamblin and P. Mróz, Artech House engineering in medicine & biology series, Artech House, Boston, Mass, 2008.
5 K. Plaetzer, B. Krammer, J. Berlanda, F. Berr and T. Kiesslich, Photophysics and Photochemistry of Photodynamic Therapy: Fundamental Aspects, *Laser Med. Sci.*, 2009, **24**(2), 259–268, DOI: 10.1007/s10103-008-0539-1.
6 P. Agostinis, K. Berg, K. A. Cengel, T. H. Foster, A. W. Girotti, S. O. Gollnick, S. M. Hahn, M. R. Hamblin, A. Juzeniene, D. Kessel, M. Korbelik, J. Moan, P. Mroz, D. Nowis, J. Piette, B. C. Wilson and J. Golab, Photodynamic Therapy of Cancer: An Update, *Ca - Cancer J. Clin.*, 2011, **61**(4), 250–281, DOI: 10.3322/caac.20114.
7 *Handbook of Photomedicine*, ed. M. R. Hamblin and Y.-Y. Huang, CRC Press, Boca Raton, FL, 2014.
8 R. R. Allison, Photodynamic Therapy: Oncologic Horizons, *Future Oncol.*, 2014, **10**(1), 123–124, DOI: 10.2217/fon.13.176.
9 L. Benov, Photodynamic Therapy: Current Status and Future Directions, *Med. Princ. Pract.*, 2015, **24**(suppl. 1), 14–28, DOI: 10.1159/000362416.
10 *Photodynamic Medicine: From Bench to Clinic*, ed. H. Kostron and T. Hasan, Comprehensive series in photochmistry and photobiology, Royal Society of Chemistry, Great Britain, Cambridge, 2016.
11 H. Abrahamse and M. R. Hamblin, New Photosensitizers for Photodynamic Therapy, *Biochem. J.*, 2016, **473**(4), 347–364, DOI: 10.1042/BJ20150942.
12 D. van Straten, V. Mashayekhi, H. de Bruijn, S. Oliveira and D. Robinson, Oncologic Photodynamic Therapy: Basic Principles, Current Clinical Status and Future Directions, *Cancers*, 2017, **9**(12), 19, DOI: 10.3390/cancers9020019.
13 S. Monro, K. L. Colón, H. Yin, J. Roque, P. Konda, S. Gujar, R. P. Thummel, L. Lilge, C. G. Cameron and S. A. McFarland, Transition Metal Complexes and Photodynamic Therapy from a Tumor-Centered Approach: Challenges, Opportunities, and Highlights from the Development of TLD1433, *Chem. Rev.*, 2019, **119**(2), 797–828, DOI: 10.1021/acs.chemrev.8b00211.
14 G. Shafirstein, D. Bellnier, E. Oakley, S. Hamilton, M. Potasek, K. Beeson and E. Parilov, Interstitial Photodynamic Therapy—A Focused Review, *Cancers*, 2017, **9**(12), 12, DOI: 10.3390/cancers9020012.
15 B. W. Henderson, S. O. Gollnick, J. W. Snyder, T. M. Busch, P. C. Kousis, R. T. Cheney and J. Morgan, Choice of Oxygen-Conserving Treatment Regimen Determines the Inflammatory Response and Outcome of Photodynamic Therapy of Tumors, *Cancer Res.*, 2004, **64**(6), 2120–2126.
16 M. Shams, B. Owczarczak, P. Manderscheid-Kern, D. A. Bellnier and S. O. Gollnick, Development of Photodynamic Therapy Regimens That Control Primary Tumor Growth and Inhibit Secondary Disease, *Cancer Immunol. Immunother.*, 2015, **64**(3), 287–297, DOI: 10.1007/s00262-014-1633-9.
17 S. O. Gollnick, L. Vaughan and B. W. Henderson, Generation of Effective Antitumor Vaccines Using Photodynamic Therapy, *Cancer Res.*, 2002, **62**(6), 1604–1608.

18 A. P. Castano, P. Mroz and M. R. Hamblin, Photodynamic Therapy and Anti-Tumour Immunity, *Nat. Rev. Cancer*, 2006, **6**(7), 535–545, DOI: 10.1038/nrc1894.

19 S. O. Gollnick and C. M. Brackett, Enhancement of Anti-Tumor Immunity by Photodynamic Therapy, *Immunol. Res.*, 2010, **46**(1–3), 216–226, DOI: 10.1007/s12026-009-8119-4.

20 S. O. Gollnick, Photodynamic Therapy and Antitumor Immunity, *J. Natl. Compr. Canc. Netw.*, 2012, **10**(Suppl. 2), S40–S43.

21 E. Reginato, Immune Response after Photodynamic Therapy Increases Anti-Cancer and Anti-Bacterial Effects, *World J. Immunol.*, 2014, **4**(1), 1–11, DOI: 10.5411/wji.v4.i1.1.

22 F. Vatansever and M. R. Hamblin, Photodynamic Therapy and Antitumor Immune Response, in *Cancer Immunology*, ed. N. Rezaei, Springer Berlin Heidelberg, Berlin, Heidelberg, 2015, pp. 383–399, DOI: 10.1007/978-3-662-44946-2_21.

23 Y. Yang, Y. Hu and H. Wang, Targeting Antitumor Immune Response for Enhancing the Efficacy of Photodynamic Therapy of Cancer: Recent Advances and Future Perspectives, *Oxid. Med. Cell. Longevity*, 2016, **2016**, 1–11, DOI: 10.1155/2016/5274084.

24 H. S. Hwang, H. Shin, J. Han and K. Na, Combination of Photodynamic Therapy (PDT) and Anti-Tumor Immunity in Cancer Therapy, *J. Pharm. Invest.*, 2018, **48**(2), 143–151, DOI: 10.1007/s40005-017-0377-x.

25 M. Korbelik, Role of Cell Stress Signaling Networks in Cancer Cell Death and Antitumor Immune Response Following Proteotoxic Injury Inflicted by Photodynamic Therapy: TUMOR AND HOST RESPONSE TO PDT AND BCG, *Laser Surg. Med.*, 2018, **50**(5), 491–498, DOI: 10.1002/lsm.22810.

26 M. Kaleta-Richter, A. Kawczyk-Krupka, D. Aebisher, D. Bartusik-Aebisher, Z. Czuba and G. Cieślar, The Capability and Potential of New Forms of Personalized Colon Cancer Treatment: Immunotherapy and Photodynamic Therapy, *Photodiagnosis Photodyn. Ther.*, 2019, **25**, 253–258, DOI: 10.1016/j.pdpdt.2019.01.004.

27 S. Nath, G. Obaid and T. Hasan, The Course of Immune Stimulation by Photodynamic Therapy: Bridging Fundamentals of Photochemically Induced Immunogenic Cell Death to the Enrichment of T-Cell Repertoire, *Photochem. Photobiol.*, 2019, **95**(6), 1288–1305, DOI: 10.1111/php.13173.

28 R. Falk-Mahapatra and S. O. Gollnick, Photodynamic Therapy and Immunity: An Update, *Photochem. Photobiol.*, 2020, 13253, DOI: 10.1111/php.13253.

29 FDA, *Highlights of Prescribing Information for Photofrin (Porfimer Sodium) Injection*, FDA, April 2011.

30 M. H. Abdel-Kader, History of Photodynamic Therapy, in *Photodynamic Therapy*, ed. M. H. Abdel-Kader, Springer Berlin Heidelberg, Berlin, Heidelberg, 2014, pp. 3–22. DOI: 10.1007/978-3-642-39629-8_1.

31 J. Levy and E. Levy, Photofrin-PDT from Bench to Bedside: Some Lessons Learned, in *Handbook of photodynamic therapy: updates on recent applications of porphyrin-based compounds*, ed. R. K. Pandey, D. Kessel and T. J. Dougherty, World Scientific, New Jersey, 2016.

32 D. T. J. D. Kessel, An Appreciation, *Photochem. Photobiol.*, 2020, **96**(3), 454–457, DOI: 10.1111/php.13144.

33 E. D. Sternberg and D. Dolphin, Second Generation Photodynamic Agents: A Review, *J. Clin. Laser Med. Surg.*, 1993, **11**(5), 233–241, DOI: 10.1089/clm.1993.11.233.

34 A. Ormond and H. Freeman, Dye Sensitizers for Photodynamic Therapy, *Materials*, 2013, **6**(3), 817–840, DOI: 10.3390/ma6030817.

35 V. Rapozzi and G. Jori, Basic and Clinical Aspects of Photodynamic Therapy, in *Resistance to Photodynamic Therapy in Cancer*, ed. V. Rapozzi and G. Jori, Resistance to Targeted Anti-Cancer Therapeutics, Springer International Publishing, Cham, 2015, vol. 5, pp. 3–26, DOI: 10.1007/978-3-319-12730-9_1.

36 H. Kataoka, H. Nishie, N. Hayashi, M. Tanaka, A. Nomoto, S. Yano and T. Joh, New Photodynamic Therapy with Next-Generation Photosensitizers, *Ann. Transl. Med.*, 2017, **5**(8), 183, DOI: 10.21037/atm.2017.03.59.

37 J. Zhang, C. Jiang, J. P. Figueiró Longo, R. B. Azevedo, H. Zhang and L. A. Muehlmann, An Updated Overview on the Development of New Photosensitizers for Anticancer Photodynamic Therapy, *Acta Pharm. Sin. B*, 2018, **8**(2), 137–146, DOI: 10.1016/j.apsb.2017.09.003.

38 S. A. McFarland, A. Mandel, R. Dumoulin-White and G. Gasser, Metal-Based Photosensitizers for Photodynamic Therapy: The Future of Multimodal Oncology?, *Curr. Opin. Chem. Biol.*, 2020, **56**, 23–27, DOI: 10.1016/j.cbpa.2019.10.004.

39 T. M. Chou, K. W. Woodburn, W.-F. Cheong, S. A. Lacy, K. Sudhir, D. C. Adelman and D. Wahr, Photodynamic Therapy: Applications in Atherosclerotic Vascular Disease with Motexafin Lutetium, *Cathet. Cardiovasc. Interv.*, 2002, **57**(3), 387–394, DOI: 10.1002/ccd.10336.

40 R. R. Allison, T. S. Mang, B. D. Wilson and V. Vongtama, Tin Ethyl Etiopurpurin—Induced Photodynamic Therapy for the Treatment of Human Immunodeficiency Virus—Associated Kaposi's Sarcoma, *Curr. Ther. Res.*, 1998, **59**(1), 23–27, DOI: 10.1016/S0011-393X(98)85020-0.

41 V. D. Turubanova, I. V. Balalaeva, T. A. Mishchenko, E. Catanzaro, R. Alzeibak, N. N. Peskova, I. Efimova, C. Bachert, E. V. Mitroshina, O. Krysko, M. V. Vedunova and D. V. Krysko, Immunogenic Cell Death Induced by a New Photodynamic Therapy Based on Photosens and Photodithazine, *J. Immunother. Cancer*, 2019, **7**(1), 350, DOI: 10.1186/s40425-019-0826-3.

42 A.-R. Azzouzi, E. Barret, C. M. Moore, A. Villers, C. Allen, A. Scherz, G. Muir, M. de Wildt, N. J. Barber, S. Lebdai and M. Emberton, TOOKAD ® Soluble Vascular-Targeted Photodynamic (VTP) Therapy: Determination of Optimal Treatment Conditions and Assessment of Effects in Patients with Localised Prostate Cancer: TOOKAD ® Soluble Vascular Targeted Photodynamic (VTP) Therapy in Patients with Localised Prostate Cancer, *BJU Int.*, 2013, **112**(6), 766–774, DOI: 10.1111/bju.12265.

43 N. A. Smith and P. J. Sadler, Photoactivatable Metal Complexes: From Theory to Applications in Biotechnology and Medicine, *Philos. Trans. R. Soc., A*, 2013, **371**(1995), 20120519, DOI: 10.1098/rsta.2012.0519.

44 A. Bahreman, J.-A. Cuello-Garibo and S. Bonnet, Yellow-Light Sensitization of a Ligand Photosubstitution Reaction in a Ruthenium Polypyridyl Complex Covalently Bound to a Rhodamine Dye, *Dalton Trans.*, 2014, **43**(11), 4494–4505, DOI: 10.1039/c3dt52643g.

45 J. D. Knoll, B. A. Albani and C. Turro, New Ru(II) Complexes for Dual Photoreactivity: Ligand Exchange and 1O2 Generation, *Acc. Chem. Res.*, 2015, **48**(8), 2280–2287, DOI: 10.1021/acs.accounts.5b00227.

46 C. Mari, H. Huang, R. Rubbiani, M. Schulze, F. Würthner, H. Chao and G. Gasser, Evaluation of Perylene Bisimide-Based Ru ^{II} and Ir ^{III} Complexes as Photosensitizers for Photodynamic Therapy: Evaluation of Perylene Bisimide-Based Ru ^{II} and Ir ^{III} Complexes as Photosensitizers for Photodynamic Therapy, *Eur. J. Inorg. Chem.*, 2017, **2017**(12), 1745–1752, DOI: 10.1002/ejic.201600516.

47 W. Sun, S. Li, B. Häupler, J. Liu, S. Jin, W. Steffen, U. S. Schubert, H.-J. Butt, X.-J. Liang and S. Wu, An Amphiphilic Ruthenium Polymetallodrug for Combined Photodynamic Therapy and Photochemotherapy In Vivo, *Adv. Mater.*, 2017, **29**(6), 1603702, DOI: 10.1002/adma.201603702.

48 F. E. Poynton, S. A. Bright, S. Blasco, D. C. Williams, J. M. Kelly and T. Gunnlaugsson, The Development of Ruthenium(ii) Polypyridyl Complexes and Conjugates for *in Vitro* Cellular and *in Vivo* Applications, *Chem. Soc. Rev.*, 2017, **46**(24), 7706–7756, DOI: 10.1039/C7CS00680B.

49 F. Heinemann, J. Karges and G. Gasser, Critical Overview of the Use of Ru(II) Polypyridyl Complexes as Photosensitizers in One-Photon and Two-Photon Photodynamic Therapy, *Acc. Chem. Res.*, 2017, **50**(11), 2727–2736, DOI: 10.1021/acs.accounts.7b00180.

50 J. Liu, C. Zhang, T. W. Rees, L. Ke, L. Ji and H. Chao, Harnessing Ruthenium(II) as Photodynamic Agents: Encouraging Advances in Cancer Therapy, *Coord. Chem. Rev.*, 2018, **363**, 17–28, DOI: 10.1016/j.ccr.2018.03.002.

51 D. Havrylyuk, M. Deshpande, S. Parkin and E. C. Glazer, Ru(II) Complexes with Diazine Ligands: Electronic Modulation of the Coordinating Group Is Key to the Design of "Dual Action" Photoactivated Agents, *Chem. Commun.*, 2018, **54**(88), 12487–12490, DOI: 10.1039/c8cc05809a.

52 L. M. Loftus, K. F. Al-Afyouni, T. N. Rohrabaugh, J. C. Gallucci, C. E. Moore, J. J. Rack and C. Turro, Unexpected Role of Ru(II) Orbital and Spin Contribution on Photoinduced Ligand Exchange: New Mechanism To Access the Photodynamic Therapy Window, *J. Phys. Chem. C*, 2019, **123**(16), 10291–10299, DOI: 10.1021/acs.jpcc.9b01576.

53 J. Karges, O. Blacque, M. Jakubaszek, B. Goud, P. Goldner and G. Gasser, Systematic Investigation of the Antiproliferative Activity of a Series of Ruthenium Terpyridine Complexes, *J. Inorg. Biochem.*, 2019, **198**, 110752, DOI: 10.1016/j.jinorgbio.2019.110752.

54 V. H. S. van Rixel, V. Ramu, A. B. Auyeung, N. Beztsinna, D. Y. Leger, L. N. Lameijer, S. T. Hilt, S. E. Le Dévédec, T. Yildiz, T. Betancourt, M. B. Gildner, T. W. Hudnall, V. Sol, B. Liagre, A. Kornienko and S. Bonnet, Photo-Uncaging of a Microtubule-Targeted Rigidin Analogue in Hypoxic Cancer Cells and in a Xenograft Mouse Model, *J. Am. Chem. Soc.*, 2019, **141**(46), 18444–18454, DOI: 10.1021/jacs.9b07225.

55 D. Havrylyuk, K. Stevens, S. Parkin and E. C. Glazer, Toward Optimal Ru(II) Photocages: Balancing Photochemistry, Stability, and Biocompatibility Through Fine Tuning of Steric, Electronic, and Physiochemical Features, *Inorg. Chem.*, 2020, **59**(2), 1006–1013, DOI: 10.1021/acs.inorgchem.9b02065.

56 I. M. Dixon, E. Lebon, P. Sutra and A. Igau, Luminescent Ruthenium–Polypyridine Complexes & Phosphorus Ligands: Anything but a Simple Story, *Chem. Soc. Rev.*, 2009, **38**(6), 1621, DOI: 10.1039/b804763b.

57 A. Breivogel, M. Meister, C. Förster, F. Laquai and K. Heinze, Excited State Tuning of Bis(Tridentate) Ruthenium(II) Polypyridine Chromophores by Push-Pull Effects and Bite Angle Optimization: A Comprehensive Experimental and Theoretical Study, *Chem. - Eur. J.*, 2013, **19**(41), 13745–13760, DOI: 10.1002/chem.201302231.

58 C. A. Bignozzi, R. Argazzi, R. Boaretto, E. Busatto, S. Carli, F. Ronconi and S. Caramori, The Role of Transition Metal Complexes in Dye Sensitized Solar Devices, *Coord. Chem. Rev.*, 2013, **257**(9–10), 1472–1492, DOI: 10.1016/j.ccr.2012.09.008.

59 C. K. Prier, D. A. Rankic and D. W. C. MacMillan, Visible Light Photoredox Catalysis with Transition Metal Complexes: Applications in Organic Synthesis, *Chem. Rev.*, 2013, **113**(7), 5322–5363, DOI: 10.1021/cr300503r.

60 K.-C. Chang, S.-S. Sun, M. O. Odago and A. J. Lees, Anion Recognition and Sensing by Transition-Metal Complexes with Polarized N H Recognition Motifs, *Coord. Chem. Rev.*, 2015, **284**, 111–123, DOI: 10.1016/j.ccr.2014.09.009.

61 Q. Sun, S. Mosquera-Vazquez, Y. Suffren, J. Hankache, N. Amstutz, L. M. Lawson Daku, E. Vauthey and A. Hauser, On the Role of Ligand-Field States for the Photophysical Properties of Ruthenium(II) Polypyridyl Complexes, *Coord. Chem. Rev.*, 2015, **282–283**, 87–99, DOI: 10.1016/j.ccr.2014.07.004.

62 G. Li, L. Sun, L. Ji and H. Chao, Ruthenium(ii) Complexes with Dppz: From Molecular Photoswitch to Biological Applications, *Dalton Trans.*, 2016, **45**(34), 13261–13276, DOI: 10.1039/C6DT01624C.

63 D. Luo, K. A. Carter, D. Miranda and J. F. Lovell, Chemophototherapy: An Emerging Treatment Option for Solid Tumors, *Adv. Sci.*, 2017, **4**(1), 1600106, DOI: 10.1002/advs.201600106.

64 J. K. White, R. H. Schmehl and C. Turro, An Overview of Photosubstitution Reactions of Ru(II) Imine Complexes and Their Application in Photobiology and Photodynamic

Therapy, *Inorg. Chim. Acta.*, 2017, **454**, 7–20, DOI: 10.1016/j.ica.2016.06.007.

65 P. M. Keane and J. M. Kelly, Transient Absorption and Time-Resolved Vibrational Studies of Photophysical and Photochemical Processes in DNA-Intercalating Polypyridyl Metal Complexes or Cationic Porphyrins, *Coord. Chem. Rev.*, 2018, **364**, 137–154, DOI: 10.1016/j.ccr.2018.02.018.

66 A. B. Aletti, D. M. Gillen and T. Gunnlaugsson, Luminescent/Colorimetric Probes and (Chemo-) Sensors for Detecting Anions Based on Transition and Lanthanide Ion Receptor/Binding Complexes, *Coord. Chem. Rev.*, 2018, **354**, 98–120, DOI: 10.1016/j.ccr.2017.06.020.

67 T. Mede, M. Jäger and U. S. Schubert, "Chemistry-on-the-Complex": Functional Ru ^{II} Polypyridyl-Type Sensitizers as Divergent Building Blocks, *Chem. Soc. Rev.*, 2018, **47**(20), 7577–7627, DOI: 10.1039/c8cs00096d.

68 L. K. McKenzie, H. E. Bryant and J. A. Weinstein, Transition Metal Complexes as Photosensitisers in One- and Two-Photon Photodynamic Therapy, *Coord. Chem. Rev.*, 2019, **379**, 2–29, DOI: 10.1016/j.ccr.2018.03.020.

69 A. Juris, V. Balzani, F. Barigelletti, S. Campagna, P. Belser and A. von Zelewsky, Ru(II) Polypyridine Complexes: Photophysics, Photochemistry, Eletrochemistry, and Chemiluminescence, *Coord. Chem. Rev.*, 1988, **84**, 85–277, DOI: 10.1016/0010-8545(88)80032-8.

70 K. Kalyanasundaram, *Photochemistry of Polypyridine and Pophyrin Complexes*, Acad. Pr, London, 1992.

71 V. Balzani, A. Juris, M. Venturi, S. Campagna and S. Serroni, Luminescent and Redox-Active Polynuclear Transition Metal Complexes †, *Chem. Rev.*, 1996, **96**(2), 759–834, DOI: 10.1021/cr941154y.

72 V. Balzani, A. Credi and M. Venturi, Photochemistry and Photophysics of Coordination Compounds: An Extended View, *Coord. Chem. Rev.*, 1998, **171**, 3–16, DOI: 10.1016/S0010-8545(98)90005-4.

73 V. Balzani and A. Juris, Photochemistry and Photophysics of Ru(II)polypyridine Complexes in the Bologna Group. From Early Studies to Recent Developments, *Coord. Chem. Rev.*, 2001, **211**(1), 97–115, DOI: 10.1016/S0010-8545(00)00274-5.

74 N. D. McClenaghan, Y. Leydet, B. Maubert, M. T. Indelli and S. Campagna, Excited-State Equilibration: A Process Leading to Long-Lived Metal-to-Ligand Charge Transfer Luminescence in Supramolecular Systems, *Coord. Chem. Rev.*, 2005, **249**(13–14), 1336–1350, DOI: 10.1016/j.ccr.2004.12.017.

75 S. Campagna, F. Puntoriero, F. Nastasi, G. Bergamini and V. Balzani, Photochemistry and Photophysics of Coordination Compounds: Ruthenium, in *Photochemistry and Photophysics of Coordination Compounds I*, ed. V. Balzani and S. Campagna, Springer Berlin Heidelberg, Berlin, Heidelberg, 2007, vol. 280, pp. 117–214, DOI: 10.1007/128_2007_133.

76 Y. Liu, R. Hammitt, D. A. Lutterman, L. E. Joyce, R. P. Thummel and C. Turro, Ru(II) Complexes of New Tridentate Ligands: Unexpected High Yield of Sensitized ^{1}O $_2$, *Inorg. Chem.*, 2009, **48**(1), 375–385, DOI: 10.1021/ic801636u.

77 Y. Sun, L. E. Joyce, N. M. Dickson and C. Turro, Efficient DNA Photocleavage by [Ru(Bpy)2(Dppn)]2+ with Visible Light, *Chem. Commun.*, 2010, **46**(14), 2426, DOI: 10.1039/b925574e.

78 R. Lincoln, L. Kohler, S. Monro, H. Yin, M. Stephenson, R. Zong, A. Chouai, C. Dorsey, R. Hennigar, R. P. Thummel and S. A. McFarland, Exploitation of Long-Lived ^{3} IL Excited States for Metal–Organic Photodynamic Therapy: Verification in a Metastatic Melanoma Model, *J. Am. Chem. Soc.*, 2013, **135**(45), 17161–17175, DOI: 10.1021/ja408426z.

79 B. A. Albani, B. Peña, N. A. Leed, N. A. B. G. de Paula, C. Pavani, M. S. Baptista, K. R. Dunbar and C. Turro, Marked Improvement in Photoinduced Cell Death by a New Tris-Heteroleptic Complex with Dual Action: Singlet Oxygen Sensitization and Ligand Dissociation, *J. Am. Chem. Soc.*, 2014, **136**(49), 17095–17101, DOI: 10.1021/ja508272h.

80 G. Shi, S. Monro, R. Hennigar, J. Colpitts, J. Fong, K. Kasimova, H. Yin, R. DeCoste, C. Spencer, L. Chamberlain, A. Mandel, L. Lilge and S. A. McFarland, Ru(II) Dyads Derived from α-Oligothiophenes: A New Class of Potent and Versatile Photosensitizers for PDT, *Coord. Chem. Rev.*, 2015, **282–283**, 127–138, DOI: 10.1016/j.ccr.2014.04.012.

81 C. Reichardt, S. Monro, F. H. Sobotta, K. L. Colón, T. Sainuddin, M. Stephenson, E. Sampson, J. Roque, H. Yin, J. C. Brendel, C. G. Cameron, S. McFarland and B. Dietzek, Predictive Strength of Photophysical Measurements for in Vitro Photobiological Activity in a Series of Ru(II) Polypyridyl Complexes Derived from π-Extended Ligands, *Inorg. Chem.*, 2019, **58**(5), 3156–3166, DOI: 10.1021/acs.inorgchem.8b03223.

82 N. P. Toupin, S. Nadella, S. J. Steinke, C. Turro and J. J. Kodanko, Dual-Action Ru(II) Complexes with Bulky π-Expansive Ligands: Phototoxicity without DNA Intercalation, *Inorg. Chem.*, 2020, **59**(6), 3919–3933, DOI: 10.1021/acs.inorgchem.9b03585.

83 H. Yin, M. Stephenson, J. Gibson, E. Sampson, G. Shi, T. Sainuddin, S. Monro and S. A. McFarland, Vitro Multiwavelength PDT with 3IL States: Teaching Old Molecules New Tricks, *Inorg. Chem.*, 2014, **53**(9), 4548–4559.

84 S. P. Foxon, M. A. H. Alamiry, M. G. Walker, A. J. H. M. Meijer, I. V. Sazanovich, J. A. Weinstein and J. A. Thomas, Photophysical Properties and Singlet Oxygen Production by Ruthenium(II) Complexes of Benzo[*i*]Dipyrido[3,2-*a*:2′,3′-*c*]Phenazine: Spectroscopic and TD-DFT Study, *J. Phys. Chem. A*, 2009, **113**(46), 12754–12762, DOI: 10.1021/jp906716g.

85 P. Mroz, Y.-Y. Huang, A. Szokalska, T. Zhiyentayev, S. Janjua, A.-P. Nifli, M. E. Sherwood, C. Ruzié, K. E. Borbas, D. Fan, M. Krayer, T. Balasubramanian, E. Yang, H. L. Kee, C. Kirmaier, J. R. Diers, D. F. Bocian, D. Holten, J. S. Lindsey and M. R. Hamblin, Stable Synthetic Bacteriochlorins Overcome the Resistance of Melanoma to Photodynamic Therapy, *FASEB J.*, 2010, **24**(9), 3160–3170.

86 I. Baldea and A. G. Filip, Photodynamic Therapy in Melanoma–an Update, *J. Physiol. Pharmacol.*, 2012, **63**(2), 109–118.

87 G. Zonios, A. Dimou, I. Bassukas, D. Galaris, A. Tsolakidis and E. Kaxiras, Melanin Absorption Spectroscopy: New Method for Noninvasive Skin Investigation and Melanoma Detection, *J. Biomed. Opt.*, 2008, **13**(1), 014017, DOI: 10.1117/1.2844710.

88 L. M. Davids and B. Kleemann, Combating Melanoma: The Use of Photodynamic Therapy as a Novel, Adjuvant Therapeutic Tool, *Cancer Treat Rev*, 2011, **37**(6), 465–475, DOI: 10.1016/j.ctrv.2010.11.007.

89 J. P. Tardivo, A. Del Giglio, L. H. C. Paschoal, A. S. Ito and M. S. Baptista, Treatment of Melanoma Lesions Using Methylene Blue and RL50 Light Source, *Photodiagn. Photodyn. Ther.*, 2004, **1**(4), 345–346, DOI: 10.1016/S1572-1000(05)00005-0.

90 Y.-Y. Huang, D. Vecchio, P. Avci, R. Yin, M. Garcia-Diaz and M. R. Hamblin, Melanoma Resistance to Photodynamic Therapy: New Insights, *Biol. Chem.*, 2013, **394**(2), 239–250, DOI: 10.1515/hsz-2012-0228.

91 J. S. Nelson, J. L. McCullough and M. W. Berns, Photodynamic Therapy of Human Malignant Melanoma Xenografts in Athymic Nude Mice, *J. Natl. Cancer Inst.*, 1988, **80**(1), 56–60.

92 R. Zong and R. P. Thummel, A New Family of Ru Complexes for Water Oxidation, *J. Am. Chem. Soc.*, 2005, **127**, 12802–12803, DOI: 10.1021/ja054791m.

93 R. Haberdar, *The Synthesis and Study of 4-Aza-Acridine Type Ligands and Their Ru(II) Complexes*, University of Houston, Houston, TX, 2012.

94 Y. M. Badiei, D. E. Polyansky, J. T. Muckerman, D. J. Szalda, R. Haberdar, R. Zong, R. P. Thummel and E. Fujita, Water Oxidation with Mononuclear Ruthenium(II) Polypyridine Complexes Involving a Direct Ru ^{IV} =O Pathway in Neutral and Alkaline Media, *Inorg. Chem.*, 2013, **52**(15), 8845–8850, DOI: 10.1021/ic401023w.

95 A. J. McConnell, M. H. Lim, E. D. Olmon, H. Song, E. E. Dervan and J. K. Barton, Luminescent Properties of Ruthenium(II) Complexes with Sterically Expansive Ligands Bound to DNA Defects, *Inorg. Chem.*, 2012, **51**(22), 12511–12520, DOI: 10.1021/ic3019524.

96 R. P. Thummel and Y. Jahng, Polyaza Cavity Shaped Molecules. 4. Annelated Derivatives of 2,2':6',2"-Terpyridine, *J. Org. Chem.*, 1985, **50**(14), 2407–2412, DOI: 10.1021/jo00214a001.

97 C. Wang, L. Lystrom, H. Yin, M. Hetu, S. Kilina, S. A. McFarland and W. Sun, Increasing the Triplet Lifetime and Extending the Ground-State Absorption of Biscyclometalated Ir(iii) Complexes for Reverse Saturable Absorption and Photodynamic Therapy Applications, *Dalton Trans.*, 2016, **45**(41), 16366–16378, DOI: 10.1039/c6dt02416e.

98 L. Tong, A. K. Inge, L. Duan, L. Wang, X. Zou and L. Sun, Catalytic Water Oxidation by Mononuclear Ru Complexes with an Anionic Ancillary Ligand, *Inorg. Chem.*, 2013, **52**(5), 2505–2518, DOI: 10.1021/ic302446h.

99 L. Pazderski, T. Pawlak, J. Sitkowski, L. Kozerski and E. Szłyk, ^{1}H NMR Assignment Corrections and ^{1}H, ^{13}C, ^{15}N NMR Coordination Shifts Structural Correlations in Fe(II), Ru(II) and Os(II) Cationic Complexes with 2,2′-Bipyridine and 1,10-Phenanthroline, *Magn. Reson. Chem.*, 2010, **48**, 450–457, DOI: 10.1002/mrc.2600.

100 K. Kalyanasundaram, *Photochemistry of Polypyridine and Por- Phyrin Complexes*, Academic Press, London, 1992.

101 S. Campagna, F. Puntoriero, F. Nastasi, G. Bergamini and V. Balzani, Photochemistry and Photophysics of Coordination Compounds: Ruthenium, in *Photochemistry and Photophysics of Coordination Compounds I*, ed. V. Balzani and S. Campagna, Topics in Current Chemistry, Springer Berlin Heidelberg, 2007, pp. 117–214.

102 R. P. Thummel and F. Lefoulon, Polyaza Cavity Shaped Molecules. 2. Annelated Derivatives of 2,2'-Biquinoline and the Corresponding N-Oxides, *J. Org. Chem.*, 1985, **50**(5), 666–670, DOI: 10.1021/jo00205a022.

103 R. P. Thummel and F. Lefoulon, Polyaza Cavity Shaped Molecules. 11. Ruthenium Complexes of Annelated 2,2'-Biquinoline and 2,2'-Bi-1,8-Naphthyridine, *Inorg. Chem.*, 1987, **26**(5), 675–680, DOI: 10.1021/ic00252a009.

104 R. P. Thummel and V. Hegde, Polyaza-Cavity Shaped Molecules. 14. Annelated 2-(2'-Pyridyl)Indoles, 2,2'-Biindoles, and Related Systems, *J. Org. Chem.*, 1989, **54**(7), 1720–1725, DOI: 10.1021/jo00268a040.

105 R. P. Thummel and Y. Jahng, Polyaza Cavity-Shaped Molecules. 9. Ruthenium(II) Complexes of Annelated Derivatives of 2,2':6,2"-Terpyridine and Related Systems: Synthesis, Properties, and Structure, *Inorg. Chem.*, 1986, **25**(15), 2527–2534, DOI: 10.1021/ic00235a009.

106 R. Zong and R. P. Thummel, A New Family of Ru Complexes for Water Oxidation, *J. Am. Chem. Soc.*, 2005, **127**(37), 12802–12803, DOI: 10.1021/ja054791m.

107 N. Kaveevivitchai, L. Kohler, R. Zong, M. El Ojaimi, N. Mehta and R. P. Thummel, A Ru(II) Bis-Terpyridine-like Complex That Catalyzes Water Oxidation: The Influence of Steric Strain, *Inorg. Chem.*, 2013, **52**(18), 10615–10622, DOI: 10.1021/ic4016383.

108 K. G. Chen, R. D. Leapman, G. Zhang, B. Lai, J. C. Valencia, C. O. Cardarelli, W. D. Vieira, V. J. Hearing and M. M. Gottesman, Influence of Melanosome Dynamics on Melanoma Drug Sensitivity, *J. Natl. Cancer Inst.*, 2009, **101**(18), 1259–1271, DOI: 10.1093/jnci/djp259.

109 S. Rossi, M. Cordella, C. Tabolacci, G. Nassa, D. D'Arcangelo, C. Senatore, P. Pagnotto, R. Magliozzi, A. Salvati, A. Weisz, A. Facchiano and F. Facchiano, TNF-Alpha and Metalloproteases as Key Players in Melanoma Cells Aggressiveness, *J. Exp. Clin. Canc. Res.*, 2018, **37**(1), 326, DOI: 10.1186/s13046-018-0982-1.

110 S. Lazic, P. Kaspler, G. Shi, S. Monro, T. Sainuddin, S. Forward, K. Kasimova, R. Hennigar, A. Mandel, S. McFarland and L. Lilge, Novel Osmium-Based Coordination Complexes as Photosensitizers for Panchromatic Photodynamic Therapy, *Photochem. Photobiol.*, 2017, **93**(5), 1248–1258, DOI: 10.1111/php.12767.

111 J. A. Roque III, P. C. Barrett, H. D. Cole, L. M. Lifshits, G. Shi, S. Monro, D. von Dohlen, S. Kim, N. Russo, G. Deep, C. G. Cameron, M. E. Alberto and S. A. McFarland, Breaking the Barrier: An Osmium Photosensitizer with Unprecedented Hypoxic Phototoxicity for Real World Photodynamic Therapy, *Chem. Sci.*, 2020, **11**, 9784–9806, DOI: 10.1039.D0SC03008B.

112 S. S. Lucky, K. C. Soo and Y. Zhang, Nanoparticles in Photodynamic Therapy, *Chem. Rev.*, 2015, **115**(4), 1990–2042, DOI: 10.1021/cr5004198.

113 J. Roque, D. Havrylyuk, P. C. Barrett, T. Sainuddin, J. McCain, K. Colón, W. T. Sparks, E. Bradner, S. Monro, D. Heidary, C. G. Cameron, E. C. Glazer and S. A. McFarland, Strained, Photoejecting Ru(II) Complexes That Are Cytotoxic Under Hypoxic Conditions, *Photochem. Photobiol.*, 2020, **96**(2), 327–339, DOI: 10.1111/php.13174.

114 T. Sitnik, J. Hampton and B. Henderson, Reduction of Tumour Oxygenation during and after Photodynamic Therapy in Vivo: Effects of Fluence Rate, *Br. J. Cancer*, 1998, 77(9), 1386–1394, DOI: 10.1038/bjc.1998.231.

115 B. W. Henderson, T. M. Busch and J. W. Snyder, Fluence Rate as a Modulator of PDT Mechanisms, *Laser Surg. Med.*, 2006, **38**(5), 489–493, DOI: 10.1002/lsm.20327.

116 W. J. Cottrell, A. D. Paquette, K. R. Keymel, T. H. Foster and A. R. Oseroff, Irradiance-Dependent Photobleaching and Pain in -Aminolevulinic Acid-Photodynamic Therapy of Superficial Basal Cell Carcinomas, *Clin. Cancer Res.*, 2008, **14**(14), 4475–4483, DOI: 10.1158/1078-0432.CCR-07-5199.

117 I. Rizvi, S. Anbil, N. Alagic, J. P. Celli, L. Z. Zheng, A. Palanisami, M. D. Glidden, B. W. Pogue and T. Hasan, PDT Dose Parameters Impact Tumoricidal Durability and Cell Death Pathways in a 3D Ovarian Cancer Model, *Photochem. Photobiol.*, 2013, **89**(4), 942–952, DOI: 10.1111/php.12065.

118 J. Lee, Y. Lee, L. Xu, R. White and B. A. Sullenger, Differential Induction of Immunogenic Cell Death and Interferon Expression in Cancer Cells by Structured SsRNAs, *Mol. Ther. J. Am. Soc. Gene Ther.*, 2017, **25**(6), 1295–1305, DOI: 10.1016/j.ymthe.2017.03.014.

119 A. Sistigu, T. Yamazaki, E. Vacchelli, K. Chaba, D. P. Enot, J. Adam, I. Vitale, A. Goubar, E. E. Baracco, C. Remédios, L. Fend, D. Hannani, L. Aymeric, Y. Ma, M. Niso-Santano, O. Kepp, J. L. Schultze, T. Tüting, F. Belardelli, L. Bracci, V. La Sorsa, G. Ziccheddu, P. Sestili, F. Urbani, M. Delorenzi, M. Lacroix-Triki, V. Quidville, R. Conforti, J.-P. Spano, L. Pusztai, V. Poirier-Colame, S. Delaloge, F. Penault-Llorca, S. Ladoire, L. Arnould, J. Cyrta, M.-C. Dessoliers, A. Eggermont, M. E. Bianchi, M. Pittet, C. Engblom, C. Pfirschke, X. Préville, G. Uzè, R. D. Schreiber, M. T. Chow, M. J. Smyth, E. Proietti, F. André, G. Kroemer and L. Zitvogel, Cancer Cell-Autonomous Contribution of Type I Interferon Signaling to the Efficacy of Chemotherapy, *Nat. Med.*, 2014, **20**(11), 1301–1309, DOI: 10.1038/nm.3708.

120 M. Budhwani, R. Mazzieri and R. Dolcetti, Plasticity of Type I Interferon-Mediated Responses in Cancer Therapy: From Anti-Tumor Immunity to Resistance, *Front. Oncol.*, 2018, **8**, 322, DOI: 10.3389/fonc.2018.00322.

121 L. Galluzzi, A. Buqué, O. Kepp, L. Zitvogel and G. Kroemer, Immunogenic Cell Death in Cancer and Infectious Disease, *Nat. Rev. Immunol.*, 2017, **17**(2), 97–111, DOI: 10.1038/nri.2016.107.

122 S. Gujar, R. Dielschneider, D. Clements, E. Helson, M. Shmulevitz, P. Marcato, D. Pan, L.-Z. Pan, D.-G. Ahn, A. Alawadhi and P. W. K. Lee, Multifaceted Therapeutic Targeting of Ovarian Peritoneal Carcinomatosis through Virus-Induced Immunomodulation, *Mol. Ther. J. Am. Soc. Gene Ther.*, 2013, **21**(2), 338–347, DOI: 10.1038/mt.2012.228.

123 H. Kolarova, P. Nevrelova, K. Tomankova, P. Kolar, R. Bajgar and J. Mosinger, Production of Reactive Oxygen Species after Photodynamic Therapy by Porphyrin Sensitizers, *Gen. Physiol. Biophys.*, 2008, **27**(2), 101–105.

124 H. Liang, Z. Zhou, R. Luo, M. Sang, B. Liu, M. Sun, W. Qu, F. Feng and W. Liu, Tumor-Specific Activated Photodynamic Therapy with an Oxidation-Regulated Strategy for Enhancing Anti-Tumor Efficacy, *Theranostics*, 2018, **8**(18), 5059–5071, DOI: 10.7150/thno.28344.

125 M. Yuan, C. Liu, J. Li, W. Ma, X. Yu, P. Zhang and Y. Ji, The Effects of Photodynamic Therapy on Leukemia Cells Mediated by KillerRed, a Genetically Encoded Fluorescent Protein Photosensitizer, *BMC Cancer*, 2019, **19**(1), 934, DOI: 10.1186/s12885-019-6124-0.

126 A. D. Garg, D. V. Krysko, P. Vandenabeele and P. Agostinis, DAMPs and PDT-Mediated Photo-Oxidative Stress: Exploring the Unknown, *Photochem. Photobiol. Sci.*, 2011, **10**(5), 670–680, DOI: 10.1039/c0pp00294a.

127 V. R. Wiersma, M. Michalak, T. M. Abdullah, E. Bremer and P. Eggleton, Mechanisms of Translocation of ER Chaperones to the Cell Surface and Immunomodulatory Roles in Cancer and Autoimmunity, *Front. Oncol.*, 2015, **5**, 7, DOI: 10.3389/fonc.2015.00007.

128 N. Rufo, A. D. Garg and P. Agostinis, The Unfolded Protein Response in Immunogenic Cell Death and Cancer Immunotherapy, *Trends Cancer*, 2017, **3**(9), 643–658, DOI: 10.1016/j.trecan.2017.07.002.

129 S. L. Klein and K. L. Flanagan, Sex Differences in Immune Responses, *Nat. Rev. Immunol.*, 2016, **16**(10), 626–638, DOI: 10.1038/nri.2016.90.

130 S. Gupta, M. Artomov, W. Goggins, M. Daly and H. Tsao, Gender Disparity and Mutation Burden in Metastatic Melanoma, *J. Natl. Cancer Inst.*, 2015, **107**(11), djv221, DOI: 10.1093/jnci/djv221.

131 C. R. Scoggins, M. I. Ross, D. S. Reintgen, R. D. Noyes, J. S. Goydos, P. D. Beitsch, M. M. Urist, S. Ariyan, J. J. Sussman, M. J. Edwards, A. B. Chagpar, R. C. G. Martin, A. J. Stromberg, L. Hagendoorn and K. M. McMasters, Sunbelt Melanoma Trial. Gender-Related Differences in Outcome for Melanoma Patients, *Ann. Surg.*, 2006, **243**(5), 693–698, DOI: 10.1097/01.sla.0000216771.81362.6b.

132 C. J. D. Wallis, M. Butaney, R. Satkunasivam, S. J. Freedland, S. P. Patel, O. Hamid, S. K. Pal and

Z. Klaassen, Association of Patient Sex With Efficacy of Immune Checkpoint Inhibitors and Overall Survival in Advanced Cancers: A Systematic Review and Meta-Analysis, *JAMA Oncol*, 2019, **5**(4), 529–536, DOI: 10.1001/jamaoncol.2018.5904.

133 P.-Y. Lin, L. Sun, S. R. Thibodeaux, S. M. Ludwig, R. K. Vadlamudi, V. J. Hurez, R. Bahar, M. J. Kious, C. B. Livi, S. R. Wall, L. Chen, B. Zhang, T. Shin and T. J. Curiel, B7-H1-Dependent Sex-Related Differences in Tumor Immunity and Immunotherapy Responses, *J. Immunol.*, 2010, **185**(5), 2747–2753, DOI: 10.4049/jimmunol.1000496.

134 F. Conforti, L. Pala, V. Bagnardi, T. De Pas, M. Martinetti, G. Viale, R. D. Gelber and A. Goldhirsch, Cancer Immunotherapy Efficacy and Patients' Sex: A Systematic Review and Meta-Analysis, *Lancet Oncol*, 2018, **19**(6), 737–746, DOI: 10.1016/S1470-2045(18)30261-4.

135 A. Grassadonia, I. Sperduti, P. Vici, L. Iezzi, D. Brocco, T. Gamucci, L. Pizzuti, M. Maugeri-Saccà, P. Marchetti, G. Cognetti, M. De Tursi, C. Natoli, M. Barba and N. Tinari, Effect of Gender on the Outcome of Patients Receiving Immune Checkpoint Inhibitors for Advanced Cancer: A Systematic Review and Meta-Analysis of Phase III Randomized Clinical Trials, *J. Clin. Med.*, 2018, **7**(12), DOI: 10.3390/jcm7120542.

136 A. Joosse, S. Collette, S. Suciu, T. Nijsten, P. M. Patel, U. Keilholz, A. M. M. Eggermont, J. W. W. Coebergh and E. de Vries, Sex Is an Independent Prognostic Indicator for Survival and Relapse/Progression-Free Survival in Metastasized Stage III to IV Melanoma: A Pooled Analysis of Five European Organisation for Research and Treatment of Cancer Randomized Controlled Trials, *J. Clin. Oncol.*, 2013, **31**(18), 2337–2346, DOI: 10.1200/JCO.2012.44.5031.

137 A. Joosse, S. Collette, S. Suciu, T. Nijsten, F. Lejeune, U. R. Kleeberg, J. W. W. Coebergh, A. M. M. Eggermont and E. de Vries, Superior Outcome of Women with Stage I/II Cutaneous Melanoma: Pooled Analysis of Four European Organisation for Research and Treatment of Cancer Phase III Trials, *J. Clin. Oncol.*, 2012, **30**(18), 2240–2247, DOI: 10.1200/JCO.2011.38.0584.

138 A. Micheli, R. Ciampichini, W. Oberaigner, L. Ciccolallo, E. de Vries, I. Izarzugaza, P. Zambon, G. Gatta, R. De Angelis and EUROCARE Working Group, The Advantage of Women in Cancer Survival: An Analysis of EUROCARE-4 Data, *Eur. J. Canc.*, 2009, **45**(6), 1017–1027, DOI: 10.1016/j.ejca.2008.11.008.

139 N. Duma, A. Abdel-Ghani, S. Yadav, K. P. Hoversten, C. T. Reed, A. N. Sitek, E. A. L. Enninga, J. Paludo, J. V. Aguilera, K. Leventakos, Y. Lou, L. A. Kottschade, H. Dong, A. S. Mansfield, R. Manochakian, A. A. Adjei and R. S. Dronca, Sex Differences in Tolerability to Anti-Programmed Cell Death Protein 1 Therapy in Patients with Metastatic Melanoma and Non-Small Cell Lung Cancer: Are We All Equal?, *The Oncologist*, 2019, **24**(11), e1148–e1155, DOI: 10.1634/theoncologist.2019-0094.

140 J. G. Markle and E. N. Fish, SeXX Matters in Immunity, *Trends Immunol.*, 2014, **35**(3), 97–104, DOI: 10.1016/j.it.2013.10.006.

141 I. Capone, P. Marchetti, P. A. Ascierto, W. Malorni and L. Gabriele, Sexual Dimorphism of Immune Responses: A New Perspective in Cancer Immunotherapy, *Front. Immunol.*, 2018, **9**, 552, DOI: 10.3389/fimmu.2018.00552.

142 M. Surcel, C. Constantin, C. Caruntu, S. Zurac and M. Neagu, Inflammatory Cytokine Pattern Is Sex-Dependent in Mouse Cutaneous Melanoma Experimental Model, *J. Immunol. Res.*, 2017, **2017**, 9212134, DOI: 10.1155/2017/9212134.

